JCB Journal of Cell Biology

ARTICLE

RAB3 phosphorylation by pathogenic LRRK2 impairs trafficking of synaptic vesicle precursors

Dan Dou[1,2,3], Jayne Aiken[1], and Erika L.F. Holzbaur[1,2,3]

Gain-of-function mutations in the *LRRK2* gene cause Parkinson's disease (PD), characterized by debilitating motor and non-motor symptoms. Increased phosphorylation of a subset of RAB GTPases by LRRK2 is implicated in PD pathogenesis. We find that increased phosphorylation of RAB3A, a cardinal synaptic vesicle precursor (SVP) protein, disrupts anterograde axonal transport of SVPs in iPSC-derived human neurons (iNeurons) expressing hyperactive *LRRK2*-p.R1441H. Knockout of the opposing protein phosphatase 1H (*PPM1H*) in iNeurons phenocopies this effect. In these models, the compartmental distribution of synaptic proteins is altered; synaptophysin and synaptobrevin-2 become sequestered in the neuronal soma with decreased delivery to presynaptic sites along the axon. We find that RAB3A phosphorylation disrupts binding to the motor adaptor MADD, potentially preventing the formation of the RAB3A–MADD-KIF1A/1Bβ complex driving anterograde SVP transport. RAB3A hyperphosphorylation also disrupts interactions with RAB3GAP and RAB-GDI1. Our results reveal a mechanism by which pathogenic hyperactive LRRK2 may contribute to the altered synaptic homeostasis associated with characteristic non-motor and cognitive manifestations of PD.

Introduction

Parkinson's disease (PD) is a devastating neurodegenerative disease that causes cardinal motor symptoms: rest tremor, rigidity, bradykinesia, and postural instability (Kalia and Lang, 2015). These are manifestations of the loss of select neuronal populations, most prominently dopaminergic neurons in the substantia nigra pars compacta (SNc). In addition to these motor symptoms, PD is clinically characterized by debilitating non-motor symptoms such as cognitive decline, dementia, sleep disturbance, and depression (Kalia and Lang, 2015), suggesting that pathogenic mechanisms may also alter synaptic transmission in a broader set of neuronal populations.

Autosomal dominant missense mutations in the leucine-rich repeat kinase 2 (*LRRK2*) gene are the most common genetic cause of PD, accounting for ∼5% of familial cases (Healy et al., 2008). Furthermore, genome-wide association studies have implicated *LRRK2* noncoding variants in sporadic PD. Seven gain-of-function pathogenic mutations in *LRRK2* increase LRRK2 kinase activity, resulting in elevated phosphorylation of a subset of RAB GTPases (RABs) (Steger et al., 2016). RABs coordinate vesicle trafficking by selectively associating with membrane compartments and recruiting effector proteins (Pfeffer, 2017). Mounting evidence shows that LRRK2-mediated phosphorylation of RABs alters their binding properties, either by introducing a new set of binding partners (Waschbüsch et al., 2020; Bonet-Ponce et al., 2020; Kluss et al., 2022; Boecker et al., 2021; Pal et al., 2023) or by impairing interaction with previous partners (Steger et al., 2016, 2017; Mamais et al., 2021). Therefore, the relative activity of LRRK2 and its opposing protein phosphatase 1H (PPM1H) regulates RAB binding to effectors (Dou et al., 2023; Berndsen et al., 2019).

In recent work, we demonstrated that LRRK2-mediated RAB hyperphosphorylation has consequences for retrograde axonal transport of autophagic vesicles (AVs), disrupting an interplay of motor regulators in a manner scaling with magnitude of LRRK2 kinase activity (Dou et al., 2023). Neurons require the directed transport of a wide range of distinct axonal cargoes to maintain homeostasis and synaptic function, in addition to AVs. Given the cognitive impairments and other non-motor manifestations of PD, an axonal cargo of particular interest is the synaptic vesicle precursor (SVP). SVPs arise in the neuronal soma and are transported anterogradely by kinesin-3 family members KIF1A and KIF1Bβ, carrying proteins that are fated for mature synaptic vesicles (SVs) at presynaptic sites (Nakata et al., 1998; Mundigl et al., 1993; Niwa et al., 2008, 2017; Hummel and Hoogenraad, 2021; De Pace et al., 2020; Goldstein et al., 2008), including numerous en passant synapses populating the complex axonal arbor. These SV proteins are only recycled for a limited time before being targeted for degradation, necessitating

[1]Department of Physiology, Perelman School of Medicine, University of Pennsylvania, Philadelphia, PA, USA; [2]Aligning Science Across Parkinson's (ASAP) Collaborative Research Network, Chevy Chase, MD, USA; [3]Neuroscience Graduate Group, Perelman School of Medicine, University of Pennsylvania, Philadelphia, PA, USA.

Correspondence to Erika L.F. Holzbaur: holzbaur@pennmedicine.upenn.edu.

robust delivery of new SVPs to replenish SV machinery (Truckenbrodt et al., 2018; Guedes-Dias et al., 2019).

Anterograde SVP transport is initiated by the formation of a complex between RAB3, KIF1A/1Bβ, and a protein called "differentially expressed in normal and neoplastic cells/MAP kinase activating death domain" (DENN/MADD, henceforth referred to as MADD) (Niwa et al., 2008; Hummel and Hoogenraad, 2021). All three components of this complex are essential for the rapid, long-range transport of SVPs. MADD is a large ∼183 kDa protein that is also known as RAB3-GEP (guanine nucleotide exchange protein) due to its role as a GDP-GTP exchange factor (GEF) for RAB3 (Brown and Howe, 1998). Indeed, previous work has shown that the anterograde transport of SVPs depends on the GTP-bound state of RAB3 (Niwa et al., 2008; Südhof, 1997).

RAB3 exists in four isoforms (RAB3A/B/C/D), with RAB3A being the most abundant in the brain cortex, although all four isoforms act redundantly in neurons (Schlüter et al., 2002, 2004). Importantly, all four isoforms are endogenous substrates of LRRK2 (Steger et al., 2016, 2017) and are dephosphorylated by PPM1H (Berndsen et al., 2019). However, the downstream consequences of LRRK2-mediated RAB3 phosphorylation on axonal transport have not been explored.

Here, we demonstrate that the hyperactive *LRRK2*-p.R1441H mutation reduces the anterograde axonal flux of SVPs in gene-edited iPSC-derived human neurons (iNeurons). As an orthogonal model of RAB3 hyperphosphorylation, we show that knock-out (KO) of *PPM1H* phenocopies the effect of p.R1441H KI, indicating an important balance between LRRK2 and its opposing phosphatase for the regulation of SVP transport. This transport deficit alters the distribution of SVP-associated proteins within the neuron, causing somal sequestration and decreased delivery to presynaptic sites in a heterologous synaptic model. Increasing levels of active RAB3 induced by overexpression of a GTP-locked mutant rescued the SVP transport deficit in p.R1441H KI iNeurons. Using a coimmunoprecipitation approach, we show that phosphorylation of RAB3A at the threonine 86 (T86) residue disrupts its binding to the motor adaptor protein MADD and the regulatory proteins RAB-GDI1 and RAB3GAP but does not indiscriminately disrupt interactions with other known RAB3 binding partners. Together, our results uncover a mechanism by which pathogenic hyperactive LRRK2 mutations may contribute to synaptic dysfunction manifesting as debilitating motor and non-motor PD symptoms.

Results

Endogenous LRRK2-p.R1441H impairs anterograde axonal transport of synaptic vesicle precursors

Point mutations at the p.R1441 hotspot (p.R1441C/G/H) in *LRRK2* are pathogenic for Parkinson's disease (PD) and have high penetrance (Haugarvoll et al., 2008; Klein and Westenberger, 2012; Domingo and Klein, 2018; Ruiz-Martínez et al., 2010). Previous reports have shown that these gain-of-function mutations induce hyperactivity of the LRRK2 kinase domain in multiple systems (Steger et al., 2016; Dou et al., 2023; Kalogeropulou et al., 2022) including neurogenin-2 (NGN2)-induced human neurons that express endogenous *LRRK2* (Boecker et al., 2021; Bieri et al., 2019; Fonseca-Ornelas et al., 2022). One RAB GTPase that is phosphorylated by LRRK2 is RAB3A, which is associated with SVPs (Schlüter et al., 2004) and is essential for the anterograde axonal transport of SVPs (Niwa et al., 2008; Hummel and Hoogenraad, 2021). Given reports of altered binding properties of pRABs (Steger et al., 2016; Waschbüsch et al., 2020; Bonet-Ponce et al., 2020; Kluss et al., 2022; Boecker et al., 2021; Pal et al., 2023; Steger et al., 2017), we hypothesized that *LRRK2*-p.R1441H impairs anterograde axonal SVP transport via aberrant phosphorylation of RAB3A.

To test this hypothesis, we employed human-induced pluripotent stem cells (iPSCs) with heterozygous KI of *LRRK2*-p.R1441H. These iPSCs had been gene-edited by the iPSC Neurodegenerative Disease Initiative (iNDI) at the NIH (Ramos et al., 2021) to introduce the p.R1441H mutation at the endogenous *LRRK2* locus of the KOLF2.1J parental line. Using tetracycline-inducible expression of *NGN2*, we differentiated these iPSCs into excitatory glutamatergic neurons (iNeurons) (Pantazis et al., 2022). The resulting p.R1441H KI iNeurons exhibit elevated RAB phosphorylation, as previously shown using an antibody pan-specific to multiple phosphorylated RABs including RAB3A (Dou et al., 2023). To assess SVP trafficking in these mutant iNeurons and corresponding WT control iNeurons, we live-imaged SVPs labeled by the fluorescent reporter mScarlet-synaptophysin (SYP) (Fig. 1 A). We imaged each neuron at the proximal axon to limit variability caused by axonal branchpoints at a distance of ∼100 µm from the soma to avoid the axonal initial segment. To more clearly visualize SYP+ vesicles entering the imaged axonal region, we photobleached the field of view prior to imaging to deplete pre-existing mScarlet-SYP signal in the axon (Fig. 1 A).

In WT iNeurons, we observed rapid, highly-processive SVPs traveling in the anterograde direction (Fig. 1 B). To accommodate the high speed of these vesicles, we imaged each axon at five frames per second for 5 min. We observed the anterograde population of SYP+ vesicles to be more numerous, rapid, and processive than the retrograde population (Fig. 1 B, inset), consistent with our previous observations in WT primary mouse hippocampal neurons (Guedes-Dias et al., 2019) and in WT i-Neurons from a different parental line (Aiken and Holzbaur, 2024). In *LRRK2*-p.R1441H KI iNeurons, we observed a significant decrease in anterograde SVP flux (Fig. 1, B and C). However, there was no effect on the velocity of anterograde vesicles (Fig. 1 D), indicating that SVPs that entered the axon were transported normally. We did not observe a change in the flux of retrograde SYP+ vesicles (Fig. 1 E), suggesting that the expression of mutant *LRRK2* specifically affected the anterograde population.

To confirm that this effect is dependent on LRRK2 kinase activity, we applied the selective LRRK2 kinase inhibitor MLi-2 (Fell et al., 2015) to p.R1441H KI iNeurons (Fig. 1 F). Overnight treatment with 100 nM MLi-2 rescued anterograde SVP flux (Fig. 1, G and H) without affecting anterograde velocity (Fig. 1 I). MLi-2 treatment had no effect on the flux of retrograde SYP+ vesicles (Fig. 1 J). In parallel experiments, we also examined SVP flux in i^{3}Neurons (Boecker et al., 2021; Fernandopulle et al., 2018; Boecker et al., 2020) gene-edited from the WTC11

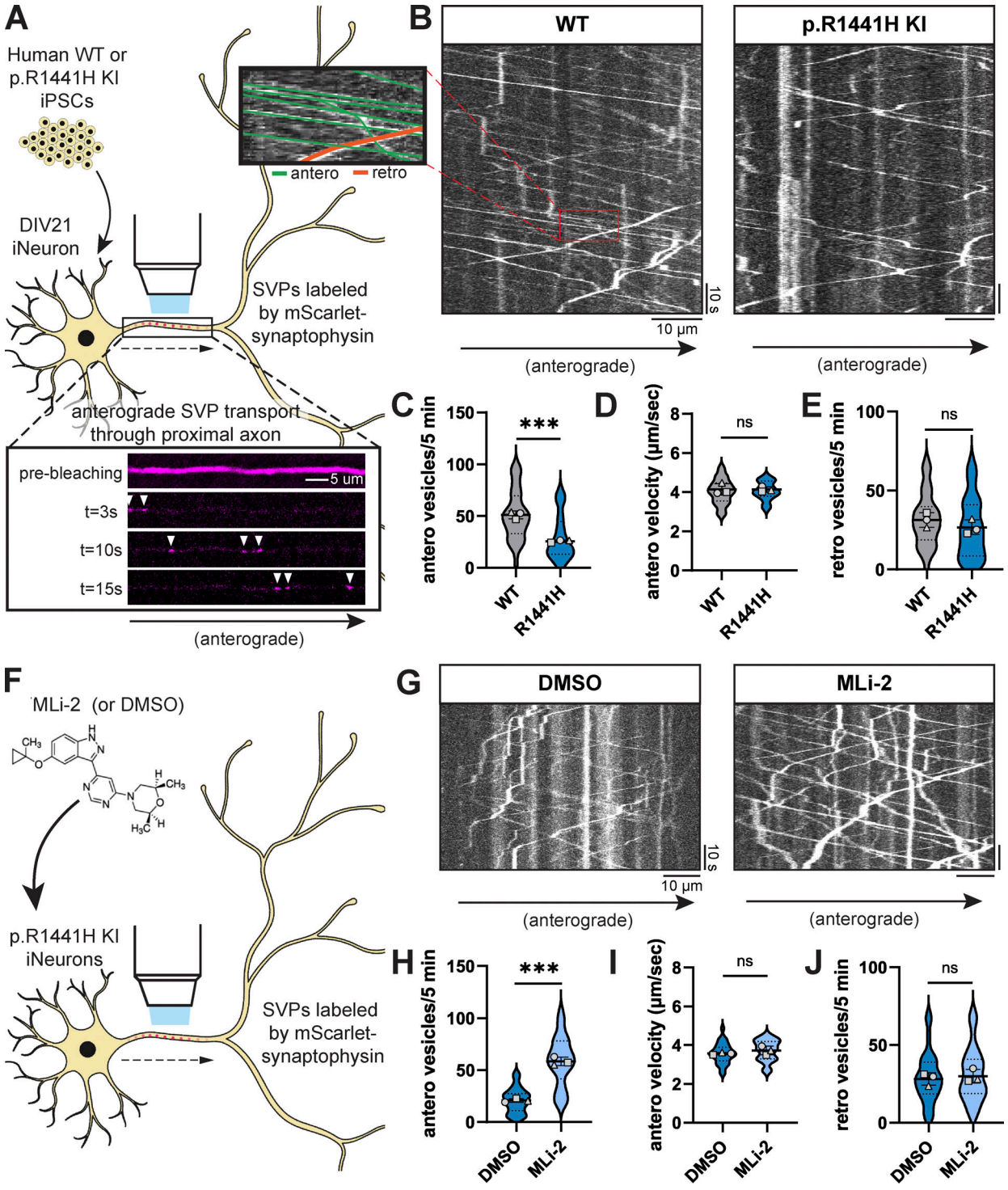

Figure 1. ***LRRK2*-p.R1441H knockin causes kinase-dependent decrease in anterograde axonal SVP flux. (A)** Inset, below: example time-lapse images of mScarlet-SYP+ vesicles in the proximal axon of a DIV21 WT iPSC-derived neuron (iNeuron). Cytoplasmic mScarlet-SYP signal was photobleached at t = 0s. **(B)** Kymographs of axonal mScarlet-SYP+ vesicles in DIV21 WT and p.R1441H KI iNeurons. Inset, left: Example traces of anterograde and retrograde SYP+ vesicles. **(C–E)** Anterograde flux (C), anterograde velocity (D), and retrograde flux (E) of SYP+ vesicles in WT and p.R1441H KI iNeurons (n = 24–33 neurons from three independent experiments; ns, not significant, P = 0.8628 for antero velocity, P = 0.2978 for retro vesicles; ***P < 0.001; linear mixed effects model). **(F)** Cartoon depicting p.R1441H KI iNeuron treated overnight with DMSO or 100 nM MLi-2. **(G)** Kymographs of axonal mScarlet-SYP+ vesicles in p.R1441H KI iNeurons treated with DMSO or MLi-2. **(H–J)** Anterograde flux (H), anterograde velocity (I), and retrograde flux (J) of SYP+ vesicles in p.R1441H KI iNeurons treated with DMSO or MLi-2 (n = 29–30 neurons from three independent experiments; ns, not significant, P = 0.2344 for antero velocity, P = 0.6735 for retro vesicles; ***P < 0.001; linear mixed effects model). Scatter plot points indicate the means of three independent experiments and error bars show the mean ± SD of these points.

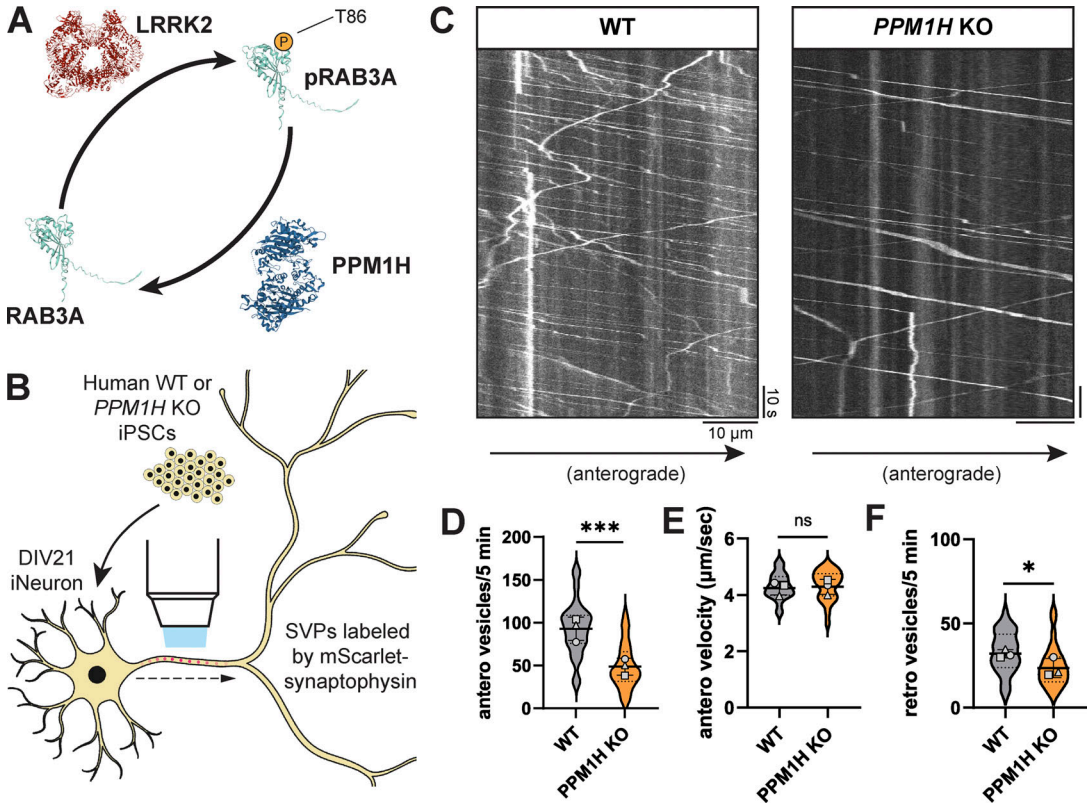

Figure 2. **Loss of LRRK2-opposing PPM1H decreases anterograde axonal SVP flux. (A)** Schematic depicting opposing regulation of RAB3A phosphorylation state at threonine 86 by LRRK2 kinase and PPM1H phosphatase. Protein structures: LRRK2 (PDB: 7LHT), PPM1H (PDB: 7L4J), RAB3A (AlphaFold prediction [Jumper et al., 2021; Varadi et al., 2022]). **(B)** Cartoon depicting WT or *PPM1H* KO iNeuron expressing mScarlet-SYP. **(C)** Kymographs of axonal mScarlet-SYP+ vesicles in DIV21 WT and *PPM1H* KO iNeurons. **(D–F)** Anterograde flux (D), anterograde velocity (E), and retrograde flux (F) of SYP+ vesicles in WT and *PPM1H* KO iNeurons (n = 28 neurons from three independent experiments; ns, not significant, P = 0.6872; *P = 0.0119; ***P < 0.001; linear mixed effects model). Scatter plot points indicate the means of three independent experiments, and error bars show mean ± SD of these points.

parental line to express the common pathological p.G2019S variant of *LRRK2*. This mutation also hyperactivates kinase activity but to a lesser extent than the p.R1441H mutation (Steger et al., 2016; Dou et al., 2023; Kalogeropulou et al., 2022). In p.G2019S KI i^{3}Neurons, we found that overnight treatment with 100 nM MLi-2 increased anterograde SVP flux compared with DMSO treatment (Fig. S1, A–C), albeit to a lesser extent than what was observed in iNeurons expressing p.R1441H.

Together, these results show a kinase activity-dependent decrease in anterograde axonal SVP flux caused by hyperactive LRRK2. Importantly, we did not observe altered anterograde SVP velocity, nor did we observe altered retrograde flux, suggesting that p.R1441H's effect is specific to decreasing the number of SVPs that enter the axon from the soma.

PPM1H KO phenocopies the effect of hyperactive LRRK2 on anterograde SVP flux in the axon

PPM1H is a phosphatase that opposes the activity of LRRK2 through dephosphorylation of RAB GTPases (Fig. 2 A) (Berndsen et al., 2019; Jumper et al., 2021; Varadi et al., 2022). Therefore, the balance of LRRK2 and PPM1H activity has the potential to regulate neuronal pathways, including the transport of axonal cargoes, by modulating RAB phosphorylation levels (Dou et al., 2023). We previously generated *PPM1H* KO iPSCs from the same KOLF2.1J parental line as the p.R1441H KI iPSCs used here (Dou et al., 2023). To determine whether loss of PPM1H would phenocopy the effect of hyperactive *LRRK2*-p.R1441H on anterograde SVP flux, we compared mScarlet-SYP motility in WT and *PPM1H* KO iNeurons (Fig. 2 B). Indeed, we observed decreased anterograde axonal flux of the SYP+ population upon loss of PPM1H (Fig. 2, C and D). Similar to observations in p.R1441H KI neurons, there was no change in anterograde velocity in *PPM1H* KO cells (Fig. 2 E). While we did observe a significant decrease in retrograde SYP+ vesicles in *PPM1H* KO iNeurons (Fig. 2 F), the size of the effect was much smaller than the effect on the anterograde population (Fig. 2 D).

In sum, these results from orthogonal models indicate that either hyperactive LRRK2 activity (Fig. 1) or knockout of the opposing phosphatase (Fig. 2) leads to decreased anterograde flux of SVPs.

RAB hyperphosphorylation alters the compartmental distribution of SVP-associated proteins

SVP transport has the important role of replenishing presynaptic sites with SV proteins (Truckenbrodt et al., 2018; Guedes-Dias et al., 2019). We next asked whether decreased anterograde transport of SVPs caused by RAB hyperphosphorylation has consequences on the distribution of synaptic proteins within the

neuron. Specifically, we interrogated the localization of two SV proteins known to be trafficked with SVPs and delivered to presynaptic sites: SYP and synaptobrevin-2 (SYB2).

To examine somal content, we stained endogenous SYP and SYB2 in p.R1441H KI and *PPM1H* KO iNeurons, as well as control WT KOLF2.1J iNeurons. An antibody to endogenous microtubule-associated protein-2 (MAP2) signal was used to visualize the somatodendritic compartment (Fig. 3 A). In both RAB-hyperphosphorylated conditions, we detected significant increases in the somal intensity of SYP (Fig. 3, A and B) and SYB2 (Fig. 3, A and C), with no associated changes in somal size, as quantified by the total area of somal MAP2 signal (Fig. S2 A). Western blots of neuronal lysates showed no evidence of changed levels of SYP, SYB2, or RAB3A (Fig. S2, B–D).

Proteins fated for SVPs are believed to be sorted at the trans-Golgi network (TGN) (Bonanomi et al., 2006; Hannah et al., 1999; Prado and Prado, 2002). We next explored whether a portion of somal SYP may be sequestered at the TGN in the context of elevated RAB3A phosphorylation. WT, p.R1441H KI, and *PPM1H* KO iNeurons were stained for endogenous SYP and golgin-97, a TGN marker (Fig. S2 E). Again, the MAP2 signal was used to visualize the somatodendritic compartment. In all three conditions, we observed that SYP intensity is enriched at the TGN relative to the whole soma (Fig. S2 F). Compared with WT neurons, *PPM1H* KO neurons displayed increased SYP intensity that colocalized with golgin-97 (Fig. S2 F). However, we did not detect this effect in p.R1441H KI iNeurons (Fig. S2 F).

Next, we sought to determine whether hyperphosphorylation of RABs disrupts the delivery of synaptic proteins to presynaptic sites. To accomplish this, we employed a recently developed heterologous synapse model for human neurons that allows unambiguous analysis of trafficking to the presynaptic compartment (Aiken and Holzbaur, 2024), introducing non-neuronal human embryonic kidney (HEK) 293T cells expressing the postsynaptic ligand neuroligin-1 (*NL1*) into coculture with iNeurons (Fig. 3 D). Within 24 h of introducing HEK cells, iNeuron axons specifically recognize *NL1*-expressing HEK cells and form connections where presynaptic proteins accumulate (Fig. 3 D, inset). This system provides both spatial and temporal control for quantification of SVP-associated protein accumulation. These heterologous presynapses contain SYP, SYB2, synapsin I/II (SYN), VGLUT1, and SVs that cycle upon neuronal depolarization (Aiken and Holzbaur, 2024). In heterologous synaptic cultures stained for endogenous SYP and SYB2 (Fig. 3 E), quantification revealed significantly decreased accumulation of both SYP (Fig. 3 F) and SYB2 (Fig. 3 G) at presynapses in *PPM1H* KO iNeurons relative to WT. In p.R1441H KI iNeurons, SYP presynaptic accumulation was also decreased, with SYB2 presynaptic accumulation trending downward but not achieving statistical significance (Fig. 3, F and G).

Together, these experiments show that the compartmental distribution of two different SVP-associated proteins is disrupted in p.R1441H KI and *PPM1H* KO iNeurons, with increased somal abundance and decreased presynaptic content. Together with our live-imaging findings, these data are consistent with somal sequestration and impaired presynaptic delivery of SVP-associated proteins as a consequence of disrupted anterograde SVP transport.

Phosphorylation of RAB3A impairs interaction with motor adaptor protein MADD

MADD has been previously shown to be essential for the transport of RAB3-containing SVPs by KIF1A and KIF1Bβ (Niwa et al., 2008). The same study showed that MADD directly interacts with KIF1A/1Bβ and RAB3. A more recent study showed that depletion of MADD levels decreased RAB3 abundance in the axon with a corresponding increase in somal sequestration (Hummel and Hoogenraad, 2021). This study further demonstrated that MADD interacts selectively with SVPs, not other axonal cargoes including dense core vesicles (DCVs) and lysosomes (Hummel and Hoogenraad, 2021). MADD is also known as RAB3-GEP (guanine nucleotide exchange protein) due to its role as a GDP-GTP exchange factor (GEF) for RAB3 (Brown and Howe, 1998). Notably, anterograde SVP transport has been shown to depend on the GTP-bound state of RAB3 (Niwa et al., 2008; Südhof, 1997). To probe the mechanism underlying *LRRK2*-p.R1441H's effect on anterograde axonal SVP flux, we first tested whether overexpressing the GTP-locked mutant of *RAB3* would rescue the deficit. Of the four RAB3 isoforms, we chose to focus on the best-characterized isoform, RAB3A, which is also the most abundant in the cortex (Schlüter et al., 2002, 2004). We found that transient expression of the glutamine-to-leucine (Q81L) mutant RAB3A, predicted to lock RAB3A into a GTP-bound state (Fig. 4 A) (Jumper et al., 2021; Varadi et al., 2022), abolished the inhibitory effect of the hyperactive LRRK2 mutant p.R1441H KI on anterograde SVP flux (Fig. 1, B and C; and Fig. 4, B–D).

It has previously been shown that LRRK2-mediated phosphorylation of RAB8A disrupts its ability to bind to RABIN8, its cognate GEF (Steger et al., 2016; Mamais et al., 2021). We therefore investigated whether the known interaction between RAB3A and MADD is altered by RAB3A phosphorylation. To test this, we coexpressed HA-MADD in HEK293T cells with EGFP-labeled RAB3A, with or without point mutations at the threonine residue that is phosphorylated by LRRK2 (Fig. 4 A) (Jumper et al., 2021; Varadi et al., 2022). Consistent with previous work (Niwa et al., 2008), $RAB3A^{WT}$ coimmunoprecipitated with MADD (Fig. 4 E). Threonine-to-alanine (T86A) mutant RAB3A, predicted to be non-phosphorylatable, exhibited the highest binding affinity to MADD (Fig. 4, E and F). Threonine-to-glutamic acid (T86E) mutant RAB3A, predicted to be a phosphomimetic, bound more weakly to MADD than $RAB3A^{WT}$ (Fig. 4, E and F).

Compared with the T86A and T86E mutants, $RAB3A^{WT}$ exhibited an intermediate binding affinity with MADD (Fig. 4, E and F). This raised the intriguing possibility that a fraction of the transiently expressed EGFP-$RAB3A^{WT}$ was phosphorylated by HEK cell endogenous $LRRK2^{WT}$ and thus exhibited an impaired ability to bind MADD. To confirm that endogenous $LRRK2^{WT}$ phosphorylates $RAB3A^{WT}$ in HEK293T cells, we applied MLi-2 prior to lysis and immunoprecipitation of EGFP-$RAB3A^{WT}$. Application of MLi-2 reduced the phosphorylated fraction of

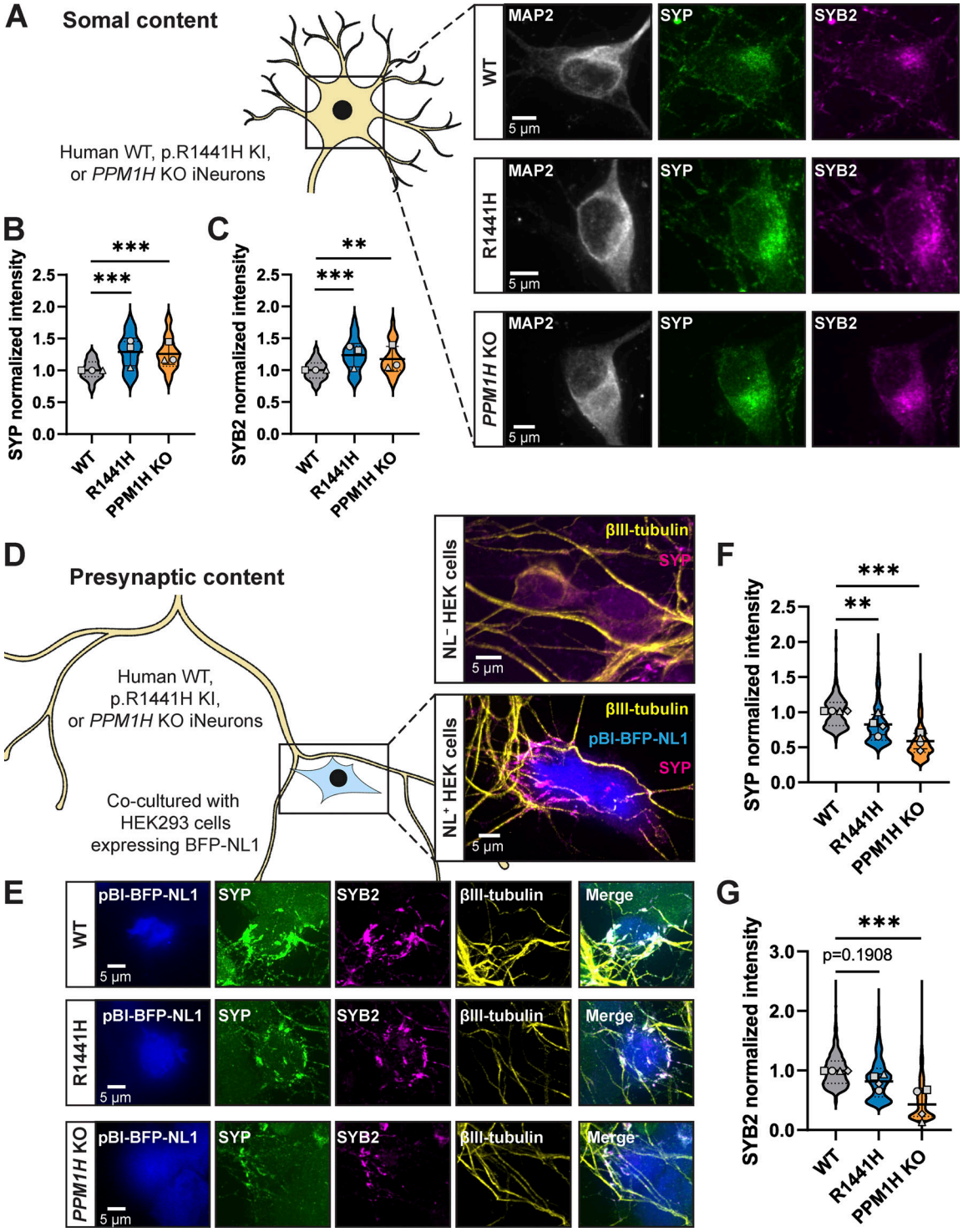

Figure 3. **Delivery of synaptic vesicle proteins from soma to presynaptic sites is disrupted by RAB hyperphosphorylation. (A)** Representative images of DIV14 WT, p.R1441H KI, and *PPM1H* KO iNeuron somas, stained for endogenous MAP2, SYP, and SYB2. **(B and C)** Normalized somal intensity (mean gray value) of SYP (B) and SYB2 (C) in WT, p.R1441H KI, and *PPM1H* KO iNeurons (n = 24 neurons from three independent experiments; **P = 0.0027; ***P < 0.001; linear mixed effects model). **(D)** Cartoon depicting heterologous synapse model set-up, where HEK293T cells expressing pBI-BFP-NL1 were introduced in coculture to WT, p.R1441H KI, or *PPM1H* KO iNeurons. Dishes were imaged at iNeuron DIV14, at which point βIII-tubulin+ iNeuron axons had selectively formed presynapses with NL1+ transfected HEK cells (inset, bottom), but not untransfected HEK cells (inset, top). **(E)** Representative images of heterologously modeled synapses including HEK293T cells expressing pBI-BFP-NL1 and WT, p.R1441H KI, or *PPM1H* KO iNeurons, stained for endogenous SYP, SYB2, and βIII-tubulin. **(F)** Normalized intensity of SYP at heterologous presynaptic sites in WT, p.R1441H KI, and *PPM1H* KO iNeurons (n = 492–840 presynaptic puncta in 17–20 fields of view from 4 independent experiments; **P = 0.0086; ***P < 0.001; linear mixed effects model). **(G)** Normalized intensity of SYB2 at heterologous presynaptic sites in WT, p.R1441H KI, and *PPM1H* KO iNeurons (n = 1,018–1,512 presynaptic puncta in 16–20 fields of view from four independent experiments; ***P < 0.001; linear mixed effects model). Scatter plot points indicate the means of three to four independent experiments, and error bars show mean ± SD of these points.

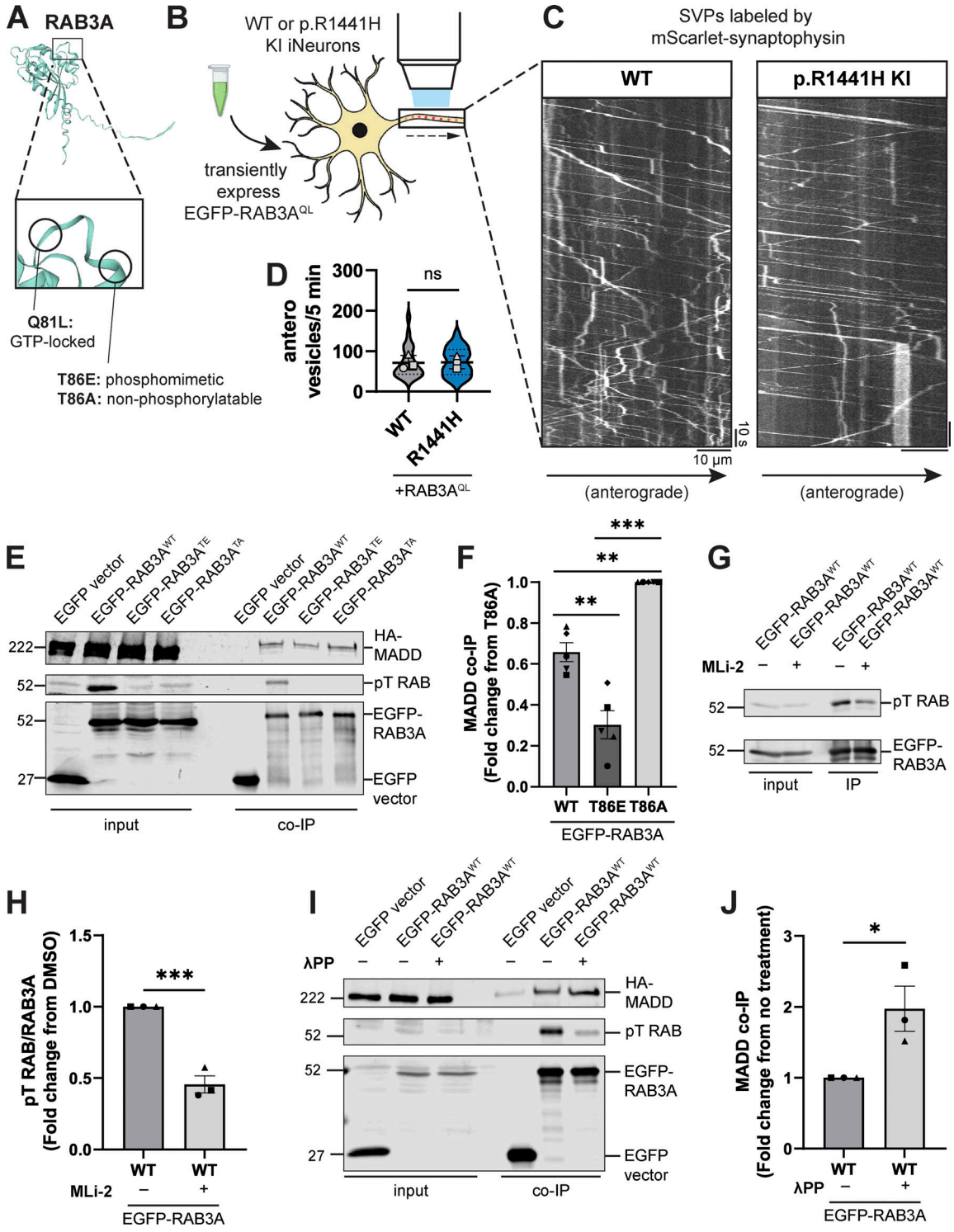

Figure 4. **Phosphorylation of RAB3A disrupts binding to motor adaptor MADD. (A)** AlphaFold prediction (Jumper et al., 2021; Varadi et al., 2022) of RAB3A. Inset illustrates locations of site-directed mutagenesis for RAB3A mutants used in this study. **(B)** Cartoon depicting experimental approach. EGFP-RAB3A^{QL} was transiently expressed in DIV21 WT or p.R1441H KI iNeurons expressing mScarlet-SYP. **(C)** Kymographs of axonal mScarlet-SYP+ vesicles in DIV21 WT and p.R1441H KI iNeurons, transiently expressing EGFP-RAB3A^{QL}. **(D)** Anterograde flux of SYP+ vesicles in WT and p.R1441H KI iNeurons, transiently expressing EGFP-RAB3A^{QL} (n = 23–24 neurons from 3 independent experiments; ns, not significant, P = 0.8993; linear mixed effects model). Scatter plot points indicate the means of three independent experiments, and error bars show mean ± SD of these points. **(E and F)** Example immunoblot and quantification of MADD coimmunoprecipitation by RAB3A^{WT}, RAB3A^{TE}, or RAB3A^{TA}, coexpressed in HEK293T cells (mean ± SEM; n = 5 independent experiments; **P = 0.0016 for WT versus T86E, P = 0.0021 for WT versus T86A; ***P < 0.0001; one-way ANOVA with Tukey's multiple comparisons test). **(G and H)** Example immunoblot and quantification of pT RAB relative to total immunoprecipitated EGFP-RAB3A^{WT}, expressed in HEK293T cells, with or without overnight treatment with 200 nM MLi-2 prior to lysis (mean ± SEM; n = 3 independent experiments; ***P = 0.0008; unpaired t test). **(I and J)** Example immunoblot and quantification of MADD coimmunoprecipitation by RAB3A^{WT}, coexpressed in HEK293T cells, with or without 30 min treatment of lysate with lambda protein phosphatase (λPP;

200 units λPP per 50 µl reaction volume) (mean ± SEM; *n* = 3 independent experiments; *P = 0.0303; unpaired *t* test). For all co-IP experiments shown, samples were processed and immunoblotted in parallel. Source data are available for this figure: SourceData F4.

RAB3A (Fig. 4, G and H), demonstrating endogenous LRRK2 activity given the high specificity of MLi-2 (Fell et al., 2015).

To confirm that phosphorylation of RAB3A^{WT} affects MADD binding, we applied lambda protein phosphatase (λPP) to lysates prior to coimmunoprecipitation of EGFP-RAB3A^{WT} and HA-MADD (Fig. 4 I). λPP treatment effectively decreased levels of phosphorylated EGFP-RAB3A^{WT} in the bound fraction and increased binding to HA-MADD (Fig. 4, I and J). In contrast, we did not observe a change in MADD binding to non-phosphorylatable RAB3A^{TA} with λPP treatment (Fig. S3).

In sum, our results show that the interaction between RAB3A and MADD is impaired by RAB3A phosphorylation at the T86 residue. Given MADD's dual role as a GEF for RAB3A and a motor adaptor for RAB3A-positive SVPs, these data suggest that impaired RAB3A–MADD interaction contributes to the deficit of anterograde SVP flux in p.R1441H KI iNeurons (Fig. 1, A–C), which can be rescued by overexpression of GTP-locked RAB3A (Fig. 4 D).

Phosphorylation of RAB3A impairs interactions with RAB-GDI1 and RAB3GAP but not RIM2 or synapsin

Multiple regulatory proteins determine RAB GTPase localization and binding state (Pfeffer, 2017). GEFs such as MADD recruit and drive the conversion of RABs to the active GTP-bound state at membranes (Brown and Howe, 1998). Each RAB functions at specific membranes, contributing to membrane identity by selective effector recruitment (Pfeffer, 2013). However, cytosolic GDP-bound RABs have been shown to be "promiscuous" in terms of their ability to enter membranes belonging to a wide range of intracellular organelles, where they may fail to encounter their cognate GEF (Gomez et al., 2019). Two regulatory proteins called RAB3 GTPase-activating protein (RAB3GAP) and RAB GDP dissociation inhibitor-1 (RAB-GDI1) act in concert to retrieve RABs from inappropriate membranes. RAB3GAP converts GTP-bound RABs to the GDP-bound state, and RAB-GDI1 serves as a chaperone to return GDP-bound RABs from membranes to the cytosol (Pfeffer, 2017). Dysregulation of the RAB GTP binding state may therefore alter subcellular RAB localization and contribute to reduced effective availability of RABs (Pfeffer, 2017, 2023).

Previous work showed that phosphomimetic mutant RAB GTPases fail to bind RAB-GDI1 and that this is also true for directly phosphorylated RAB8A^{WT} and RAB12^{WT} (Steger et al., 2016, 2017; Liu et al., 2018). Consistent with these findings, in coimmunoprecipitation experiments, we observed that the phosphomimetic T86E mutation abolished the interaction between EGFP-RAB3A and endogenous RAB-GDI1 compared with the non-phosphorylatable T86A mutant (Fig. 5, A and B). Similar to the RAB3A–MADD interaction (Fig. 4, E and F), RAB3A^{WT} exhibited intermediate binding affinity with GDI (Fig. 5, A and B). Notably, dephosphorylation of RAB3A^{WT} by λPP treatment (Fig. 5 A) significantly increased binding to RAB-GDI1 (Fig. 5, A and B), confirming that direct RAB3A phosphorylation disrupts the interaction between RAB3A and RAB-GDI1.

In the same set of coimmunoprecipitation experiments, we also explored whether phosphorylation of RAB3A disrupts binding to RAB3GAP, quantified with an antibody for the non-catalytic subunit RAB3GAP2. We noted greater non-specific binding of RAB3GAP than GDI1 to the EGFP vector (Fig. 5 A), which was subtracted prior to quantification. We observed that the binding of EGFP–RAB3A to RAB3GAP was decreased by the phosphomimetic T86E mutation compared with both RAB3A^{WT} and RAB3A^{TA} (Fig. 5, A and C). Interestingly, while the T86E mutation strongly disrupted the RAB3A-GDI1 interaction (Fig. 5, A and B), this mutation had a more moderate effect on the RAB3A-RAB3GAP interaction (Fig. 5, A and C).

RAB3A has been implicated in mechanisms of SV release, acting in concert with effector proteins (van Weering et al., 2007; Persoon et al., 2019; Huang et al., 2011). Given the effect of RAB3A phosphorylation on binding to MADD, RAB–GDI1, and RAB3GAP, we wondered if RAB3A phosphorylation indiscriminately impaired interaction with all of its effectors. We therefore tested phosphomimetic mutant RAB3A binding to RAB3A-interacting molecule 2 (RIM2) and synapsin, two presynaptic proteins that have been shown to act as RAB3A effectors (Persoon et al., 2019; Giovedì et al., 2004). In agreement with these previous reports, we observed a pulldown of both RIM2 (Fig. S4 A) and synapsin (Fig. S4 B) by RAB3A^{WT}. However, neither the phosphomimetic T86E mutation nor the non-phosphorylatable T86A mutation affected RAB3A binding to either RIM2 or synapsin, in contrast to MADD, GDI, and RAB3GAP.

In summary, our results show that RAB3A phosphorylation at T86 selectively regulates binding to a subset of partners. Binding to the regulatory chaperone protein RAB–GDI1 was strongly impaired, while moderate disruption was observed for binding to the motor adaptor MADD and the regulatory protein RAB3-GAP, and no effects were observed on binding to either RIM2 or synapsin.

Discussion

PD-linked pathogenic mutations in LRRK2 hyperphosphorylate a subset of RAB GTPases with a growing body of evidence linking this posttranslational modification to altered interactions with effectors. Though the LRRK2 substrate RAB3A has long been known to be essential for axonal SVP transport, the consequences of RAB3A phosphorylation on this trafficking pathway have not previously been explored. Here, we showed that in two iNeuron models of RAB hyperphosphorylation (*LRRK2*-p.R1441H KI and *PPM1H* KO), we observed impaired anterograde flux of SVPs (Figs. 1 and 2). We find that RAB3A phosphorylation at T86 disrupts binding to the motor adaptor protein MADD (Fig. 4). Phosphorylation of RAB3A also alters binding affinity to the regulatory proteins RAB3GAP and RAB-GDI1 (Fig. 5, A–C). Our findings support a model where pathogenic hyperactive LRRK2 causes dysregulated binding of RAB3A

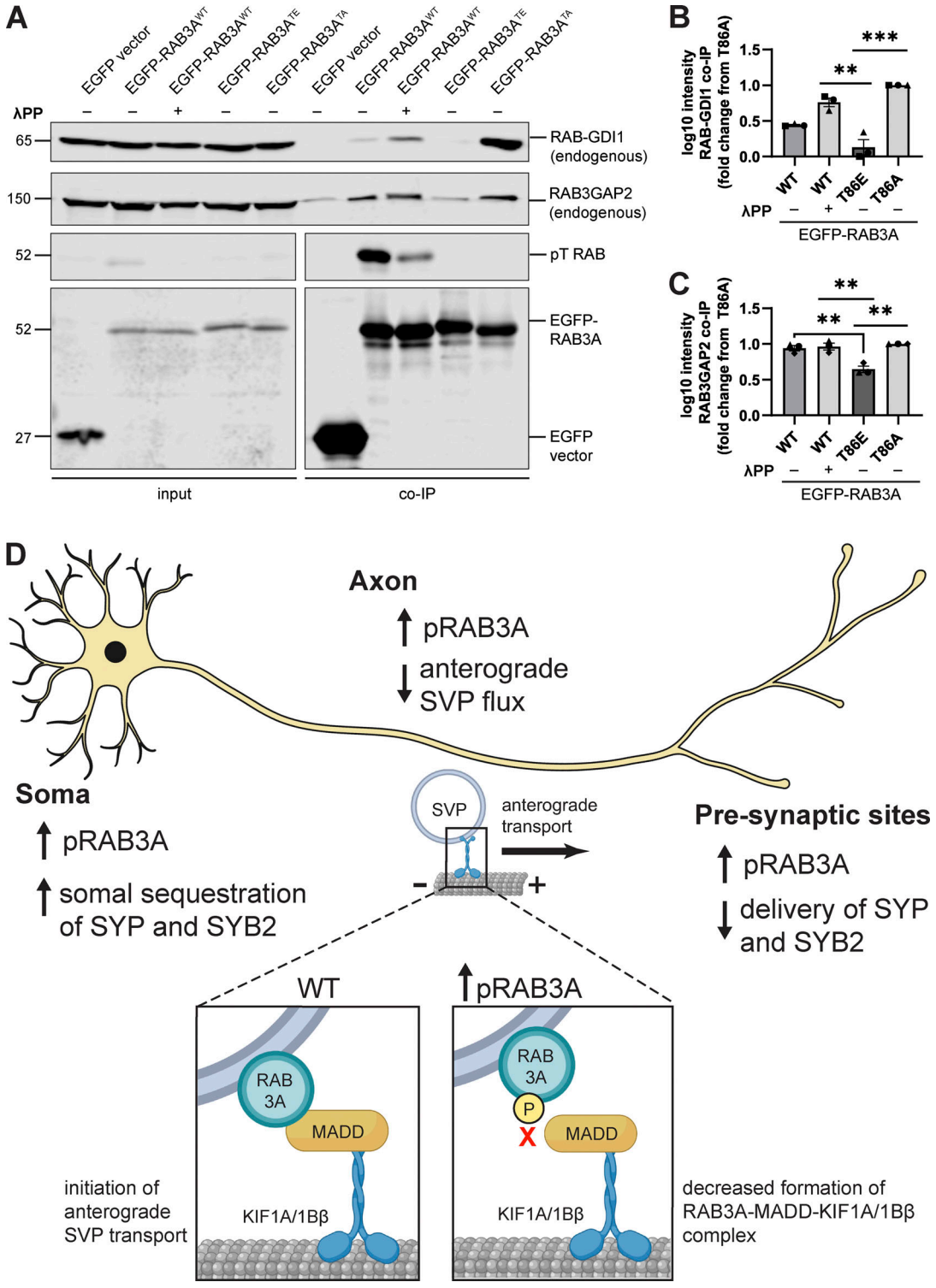

Figure 5. **Phosphorylation of RAB3A disrupts binding to RAB cycle regulators RAB-GDI1 and RAB3GAP. (A)** Example immunoblot of endogenous RAB3GAP2 and endogenous RAB-GDI1 coimmunoprecipitation by RAB3A^{WT}, RAB3A^{TE}, or RAB3A^{TA}, expressed in HEK293T cells, with or without 30 min treatment of lysate with lambda protein phosphatase (λPP; 200 units λPP per 50 µl reaction volume). Lower panels (phosphothreonine RAB and EGFP) are separated for alignment purposes; no lanes that included sample were excluded. **(B)** Quantification of endogenous RAB-GDI1 coimmunoprecipitation by RAB3A^{WT}, RAB3A^{TE}, or RAB3A^{TA}, expressed in HEK293T cells, with or without 30 min treatment of lysate with λPP (mean ± SEM; n = 3 independent experiments; **P < 0.0048; ***P < 0.001; one-way ANOVA with Tukey's multiple comparisons test). **(C)** Quantification of endogenous RAB3GAP2 coimmunoprecipitation by RAB3A^{WT}, RAB3A^{TE}, or RAB3A^{TA}, expressed in HEK293T cells, with or without 30 min treatment of lysate with λPP (mean ± SEM; n = 3 independent experiments; **P < 0.0094; one-way ANOVA with Tukey's multiple comparisons test). For all co-IP experiments shown, samples were processed and immunoblotted in parallel. **(D)** Model: Dysregulated pRAB3A binding disrupts axonal transport of SVPs and distribution of synaptic proteins. In the neuronal soma, increased phosphorylation of RAB3A by hyperactive LRRK2 results in impaired formation of the RAB3A–MADD–KIF1A/1Bβ motor complex

(inset) that is necessary for anterograde transport of SVPs out of the soma. As a result, there is increased somal sequestration of SYP and SYB2, and decreased anterograde SVP flux in the axon. Consequently, decreased SYP and SYB2 is delivered to presynaptic sites. Source data are available for this figure: SourceData F5.

in the neuronal soma, including impairment of the formation of the RAB3A–MADD–KIF1A/Bβ complex (Fig. 5 D). We hypothesize that this contributes to the reduced availability of RAB3 to stimulate anterograde SVP transport. Consistent with this hypothesis, we find that the compartmental distribution of SVP-associated proteins is disrupted within neurons with hyperphosphorylated RABs, manifesting as increased somal content and decreased delivery to presynaptic sites along the axon (Fig. 3).

Our previous work linked hyperactive LRRK2 mutations to the disruption of the retrograde axonal transport of AVs (Boecker et al., 2021; Dou et al., 2023), most likely mediated by RAB10 and/or RAB35 (Waschbüsch et al., 2020; Bonet-Ponce et al., 2020; Berndsen et al., 2019; Goldsmith et al., 2022). In contrast, hyperactive LRRK2 does not alter the axonal transport of mitochondria (Dou et al., 2023), consistent with our current understanding that there is no known role for RABs in regulating the axonal transport of these organelles. Given the altered transport of RAB3A+ SVPs, our findings indicate a high degree of RAB-dependent selectivity for which axonal cargoes are perturbed by pathogenic hyperactive LRRK2. Furthermore, because *PPM1H* KO phenocopies these transport defects, this implies that the balance between $LRRK2^{WT}$ and PPM1H may regulate the transport of both SVPs and autophagosomes under physiologic conditions. As at least 10 different RABs are endogenously phosphorylated by LRRK2 (Steger et al., 2017), it remains to be explored whether other axonal cargoes rely on RAB-mediated transport mechanisms that are regulated by LRRK2.

Recent work indicates that the subcellular colocalization of PPM1H with specific RABs strongly influences levels of RAB phosphorylation (Yeshaw et al., 2023). Regulation of RAB-mediated pathways in neurons is therefore determined by the balance of LRRK2 and PPM1H activities at each specific membrane compartment, in ways that are difficult to predict from whole-cell pRAB levels alone. While our results show that both p.R1441H KI and *PPM1H* KO affect SVP transport and synaptic protein distribution, the effect size was generally more pronounced in *PPM1H* KO neurons (Fig. 3, F and G; and Fig. S2 F). Notably, PPM1H has been shown to strongly localize to the Golgi (Berndsen et al., 2019; Yeshaw et al., 2023), suggesting that its loss may cause more striking effects on protein sorting and cargo loading at the TGN. Further work could reveal how relative LRRK2-PPM1H abundance at specific subcellular membrane compartments differentially regulates other RAB-mediated pathways.

While we observed that RAB3A phosphorylation causes strong impairment of the RAB3A-GDI1 interaction (Fig. 5, A and B), we observed only moderate impairment of RAB3A–MADD (Fig. 4, E, F, I, and J) and RAB3A-RAB3GAP (Fig. 5, A and C) binding, and no impairment of RAB3A-RIM2 (Fig. S4 A) and RAB3A-synapsin (Fig. S4 B) interaction. Together, these results predict that RAB3A phosphorylation has a spectrum of effect sizes on effector binding properties and may alter the probability of successful binding in a manner depending on the specific interfaces of protein–protein interaction. Attempts to model the RAB3A–MADD and RAB3A–GDI1 complexes with AlphaFold-Multimer (Jumper et al., 2021; Varadi et al., 2022; Evans et al., 2022, *Preprint*; Cianfrocco et al., 2017a, 2017b) proved challenging, yielding only low confidence models. However, AlphaFold-Multimer generated a relatively high-confidence model of the complex between RAB3A and RAB3-GAP1 (catalytic subunit of RAB3GAP) (Fig. S5 C; interface pTM + pTM score 0.794) (Jumper et al., 2021; Varadi et al., 2022; Evans et al., 2022, *Preprint*, 2022b; Cianfrocco et al., 2017a, 2017b). Modeling the RAB3A–MADD complex may be complicated by the presence of intrinsically disordered regions in the large MADD protein (UniProt Q8WXG6). However, previous work showed that the N-terminal 161 residues of MADD are necessary and sufficient for binding to GTP-bound RAB3 isoforms (Fig. S5 A) (Niwa et al., 2008). Moreover, MADD's motor-binding death domain region is found toward its C-terminus (Niwa et al., 2008; Hummel and Hoogenraad, 2021). RABs are phosphorylated by LRRK2 at their characteristic switch II domain, which changes conformation in response to nucleotide binding to allow for interaction with effectors or regulatory proteins (Steger et al., 2016; Pfeffer, 2005). Thus, phosphorylation of RAB3A likely disrupts interaction between the switch II region of RAB3A and the N-terminus of MADD, without interrupting MADD's ability to bind kinesin-3 (Fig. S5 A). Further work is required to elucidate the order of events and kinetics by which pRAB3A interrupts the loading of SVP cargo onto the MADD-kinesin motor complex. However, we observed that overexpression of GTP-locked RAB3A rescued anterograde SVP flux in p.R1441H KI iNeurons (Fig. 4, B–D), suggesting that increasing levels of active RAB3A in this system is sufficient to restore appropriate levels of the RAB3A–MADD–KIF1A/Bβ complex. This indicates that the increased fraction of phosphorylated RAB3A induced by p.R1441H KI reduces the abundance of eligible RAB3A required for the initiation of SVP transport.

Here, we primarily focused on the transport dynamics of the anterograde population of SYP+ vesicles, for which the mechanism of rapid, highly processive transport is known (Guedes-Dias et al., 2019). These results demonstrate that the major effect of RAB3A phosphorylation is on flux of the anterograde SYP+ population. The transport dynamics of the retrograde SYP+ population are not as well-characterized. Across multiple studies in mammalian neurons, we have observed it to be more heterogeneous, and overall less numerous, rapid, and processive than the anterograde population (Guedes-Dias et al., 2019; Aiken and Holzbaur, 2024). Recent work from our group has identified that SV proteins (including SYP and SYB2) make up a substantial proportion of autophagic cargoes (Goldsmith et al., 2022). Thus, a fraction of the retrograde SYP+ population we observe are likely to be synaptic proteins engulfed in AVs and thus moving processively in the retrograde direction along the axon.

Consistent with decreased anterograde SVP flux, our results using p.R1441H KI and *PPM1H* KO iNeurons also show decreased

accumulation of SVP-associated proteins in a temporally controlled model of presynaptic site formation (Fig. 3, D–G). Interestingly, our results are consistent with recently published work showing that inhibition of LRRK2 increases the anterograde transport of α-synuclein to the presynapse (Brzozowski et al., 2021). As α-synuclein is believed to play a role in the presynapse in modulating neurotransmitter release (Bendor et al., 2013), hyperactive LRRK2 may decrease the presynaptic delivery of α-synuclein and other proteins important for synaptic function. Given the limited effective lifespan of SVs and the need for continuous replenishment of SVPs at presynapses (Truckenbrodt et al., 2018), it is predicted that RAB hyperphosphorylation and the resulting decrease in anterograde SVP flux would be detrimental to the size and health of the SV pool, especially the readily releasable and recycling pools. However, the specific ramifications of our findings on synaptic transmission are challenging to disentangle from other roles of LRRK2 activity at the presynaptic site. Despite numerous studies using multiple model systems of LRRK2 hyperactivity or loss (reviewed extensively by Pischedda and Piccoli [Pischedda and Piccoli, 2021]), no consensus has been reached on the effect of LRRK2 on SV exocytosis. LRRK2 has been reported to interact with or regulate actin, synapsin I, SNAP25, syntaxin, NSF, endophilin A, dynamin, auxillin, and synaptojanin, all of which contribute to the SV cycle (Pischedda and Piccoli, 2021; Meixner et al., 2011; Marte et al., 2019; Yun et al., 2013; Piccoli et al., 2011, 2014; Matta et al., 2012; Stafa et al., 2014; Nguyen and Krainc, 2018; Islam et al., 2016). Furthermore, LRRK2 substrates RAB3A (van Weering et al., 2007; Persoon et al., 2019; Huang et al., 2011; Fischer von Mollard et al., 1990; Schlüter et al., 2006), RAB5 (Shimizu et al., 2003; Wucherpfennig et al., 2003; Hoopmann et al., 2010), RAB10 (Dong et al., 2024, *Preprint*; Singh et al., 2023), and RAB35 (Sheehan et al., 2016; Uytterhoeven et al., 2011) have been implicated in membrane trafficking within the presynapse. The relative balance of LRRK2 and PPM1H activity at the presynapse will likely regulate some of these interactions, but others may involve scaffolding domains of LRRK2 that are not believed to be directly kinase-dependent (Piccoli et al., 2011; Cirnaru et al., 2014). RAB-mediated pathways at the presynapse may therefore be good candidates to be differentially affected by hyperactive LRRK2. Ultimately, the effect of pathogenic LRRK2 mutations on synaptic transmission is likely an integrated function of these different interactions, with more work needed to uncover how these intersecting pathways may contribute to the development of non-motor symptoms in PD.

Materials and methods

Plasmids and reagents

Plasmids and reagents used are detailed in Table 1, along with Addgene identification numbers. Antibodies used are detailed in Table 2, along with application and dilution. CMV HA-RIM2 was derived from GST-RIM2-RBD which was a gift from Ruben Bierings (Erasmus University Medical Center, Rotterdam, Netherlands). This construct contains the first 411 amino acids of RIM2, which contains the RAB binding domain (Kat et al., 2021).

Piggybac-mediated iPSC-derived neuron differentiation

KOLF2.1J-background WT and *LRRK2*-p.R1441H KI iPSCs were a gift from B. Skarnes (The Jackson Laboratory for Genomic Medicine, Farmington, CT, USA) as part of the iPSC Neurodegenerative Disease Initiative (iNDI) and have been described previously (Pantazis et al., 2022). KOLF2.1J-background *PPM1H* KO iPSCs were generated as described previously (Dou et al., 2023). Cytogenetic analysis of G-banded metaphase cells showed a normal male karyotype (Cell Line Genetics). Mycoplasma testing was negative. iPSCs were cultured on plates coated with Growth Factor Reduced Matrigel (Corning) and fed daily with Essential 8 media (Thermo Fisher Scientific). To stably express doxycycline-inducible *hNGN2* using a PiggyBac delivery system, iPSCs were transfected with PB-TO-hNGN2 vector (gift from M. Ward, NIH, MD, USA) in a 1:2 ratio (transposase:vector) using Lipofectamine Stem (Thermo Fisher Scientific). After 72 h, transfected iPSCs were selected for 48 h with 0.5 µg/ml puromycin (Takara). Differentiation of iPSCs into iNeurons was performed using an established protocol (Pantazis et al., 2022; Fernandopulle et al., 2018). In brief, iPSCs were passaged using Accutase (Sigma-Aldrich) and plated on Matrigel-coated dishes in Induction Media (DMEM/F12 supplemented with 1% N2-supplement [Gibco], 1% NEAA [Gibco], and 1% GlutaMAX [Gibco], and containing 2 µg/ml doxycycline). After 72 h of doxycycline exposure, iNeurons were dissociated with Accutase and cryo-preserved in liquid N_2. The published protocol can be found on Protocols.io (https://doi.org/10.17504/protocols.io.e6nvwj54dlmk/v1). Recent work has found that KOLF2.1J iPSCs carry small copy number variants in *ASTN2* (Gracia-Diaz et al., 2023, *Preprint*; Ryan et al., 2024, *Preprint*). While changes in ASTN2 levels have the potential to alter synaptic strength, this is predicted to occur through postsynaptic rather than presynaptic mechanisms (Behesti et al., 2018) and is not expected to affect the phenotypes examined here.

i^{3}Neuron differentiation

Pre-i^{3}Neuron iPSCs (human iPSCs with an integrated doxycycline-inducible mNGN2 transgene in the AAVS1 safe-harbor locus) were a gift from M. Ward (NIH, MD, USA) and have been described previously (Boecker et al., 2021; Dou et al., 2023; Fernandopulle et al., 2018; Boecker et al., 2020). Cytogenetic analysis of G-banded metaphase cells showed a normal male karyotype (Cell Line Genetics). Mycoplasma testing was negative. Pre-i^{3}N iPSCs were cultured on plates coated with Growth Factor Reduced Matrigel (Corning) and fed daily with Essential 8 media (Thermo Fisher Scientific). Induction into neuronal fate with doxycycline and cryopreservation of predifferentiated neurons was performed as described above ("Piggybac-mediated iPSC-derived neuron differentiation"). The published protocol can be found on Protocols.io (https://doi.org/10.17504/protocols.io.261ge348yl47/v1).

Culture and transfection of iPSC-derived neurons

Cryo-preserved, predifferentiated iNeurons (i^{3}Neurons or Piggybac-delivered NGN2 neurons) were thawed and plated on live-imaging dishes (MatTek) coated with poly-*L*-ornithine at a density of 300,000 neurons per dish. For each experimental

Table 1. **Plasmids and reagents**

Reagent or resource	Source	Identifier
Recombinant DNA		
Plasmid: PB-TO-hNGN2	Gift from iPSC Neurodegenerative Disease Initiative (iNDI) & Michael Ward	RRID:Addgene_172115
Plasmid: PiggyBac transposase vector	Transposagen	N/A
Plasmid: PGK mScarlet-Synaptophysin	This paper	RRID:Addgene_206145
Plasmid: PGK EGFP	This paper	RRID:Addgene_216110
Plasmid: PGK EGFP-RAB3A-WT	This paper	RRID:Addgene_206146
Plasmid: PGK EGFP-RAB3A-Q81L	This paper	RRID:Addgene_206147
Plasmid: PGK EGFP-RAB3A-T86E	This paper	RRID:Addgene_206148
Plasmid: PGK EGFP-RAB3A-T86A	This paper	RRID:Addgene_206149
Plasmid: CMV HA-MADD	This paper	RRID:Addgene_206150
Plasmid: CMV HA-RIM2	This paper; GST-RIM2-RBD was a gift from Ruben Bierings (Erasmus University Medical Center) (Kat et al., 2021)	RRID:Addgene_206151
Plasmid: CMV SNAP-synapsin	This paper	RRID:Addgene_206152
Plasmid: pBI-BFP-NL1	(Aiken and Holzbaur, 2024)	RRID:Addgene_206153
Chemicals, peptides, and recombinant proteins		
MLi-2	Tocris	Cat# 5756
DMSO	Sigma-Aldrich	Cat# D2650
Matrigel growth factor reduced	Corning	Cat# 354230
Essential 8 medium	Thermo Fisher Scientific	Cat# A1517001
ReLeSR	Stemcell Technologies	Cat# 05872
Accutase	Sigma-Aldrich	Cat# A6964
ROCK inhibitor Y-27632	Selleckchem	Cat# S1049
Knockout serum replacement	Thermo Fisher Scientific	Cat# 10828010
DMEM/F-12, HEPES	Thermo Fisher Scientific	Cat# 11330032
N2 supplement	Thermo Fisher Scientific	Cat# 17502048
Non-essential amino acids (NEAA)	Thermo Fisher Scientific	Cat# 11140050
GlutaMAX	Thermo Fisher Scientific	Cat# 35050061
Doxycycline	Sigma-Aldrich	Cat# D9891
Poly-*L*-Ornithine	Sigma-Aldrich	Cat# P3655
BrainPhys neuronal medium	Stemcell Technologies	Cat# 05790
Laminin	Corning	Cat# 354232
BDNF	PeproTech	Cat# 450-02
NT-3	PeproTech	Cat# 450-03
B27 supplement	Thermo Fisher Scientific	Cat# 17504-044
Lipofectamine stem transfection reagent	Thermo Fisher Scientific	Cat# STEM00003
Microcystin-LR	Sigma-Aldrich	Cat# 475815
Halt protease and phosphatase inhibitor cocktail	Thermo Fisher Scientific	Cat# 78442
5-Fluoro-2′-deoxyuridine	Sigma-Aldrich	Cat# F0503
Uridine	Sigma-Aldrich	Cat# U3003
DMEM (Dulbecco's modified eagle's medium)	Corning	Cat# MT10-013-CV
FuGENE 6	Promega Corp	Cat# E2692
GFP-trap magnetic particles M-270	ChromoTek	Cat# gtd

Table 1. **Plasmids and reagents (*Continued*)**

Reagent or resource	Source	Identifier
GFP-trap magnetic agarose	ChromoTek	Cat# gtma
Lambda (λ) protein phosphatase	New England BioLabs	Cat# P0753S
Critical commercial assays		
BCA protein assay kit	Thermo Fisher Scientific	Cat# 23225
Plasmid maxi kit	QIAGEN	Cat# 12163
Experimental models: Cell lines		
Human: KOLF2.1J WT iPSCs	B. Skarnes (Jackson Laboratories, Connecticut)	RRID: CVCL_B5P3
Human: KOLF2.1J LRRK2-R1441H iPSCs	B. Skarnes (Jackson Laboratories, Connecticut)	N/A
Human: KOLF2.1J *PPM1H* KO iPSCs	This paper	RRID: CVCL_C7TY
Human: HEK293T	ATCC	RRID: CVCL_0063
Software and algorithms		
FIJI (release 2.9.0)	NIH, USA	http://fiji.sc, RRID:SCR_002285
Prism 9	GraphPad	https://www.graphpad.com/scientific-software/prism/, RRID:SCR_002798
RStudio: Integrated Development for R (2021.09.2 Build 382)	RStudio Team	http://www.rstudio.com/, RRID:SCR_000432
R package: nlme	Pinheiro J, Bates D, R Core Team	http://CRAN.R-project.org/package=nlme, RRID:SCR_015655
Matlab R2022a	MathWorks	https://www.mathworks.com/products/matlab.html, RRID:SCR_001622
Volocity	PerkinElmer	https://www.perkinelmer.com, RRID: SCR_002668
VisiView 5.0.0.24	Visitron	https://www.visitron.de/products/visiviewr-software.html, RRID:SCR_022546
LI-COR image studio	LI-COR	https://www.licor.com/bio/image-studio/, RRID:SCR_015795
Adobe Illustrator 2022	Adobe	https://www.adobe.com/products/illustrator.html, RRID:SCR_010279
BioRender	BioRender	https://biorender.com/, RRID:SCR_018361
Other		
35 mm #1.5 glass bottom imaging dishes	MatTek	Cat# P35G-1.5-20-C
ProLong gold antifade mountant	Thermo Fisher Scientific	Cat# P36930

condition, cells from at least two different batches of induction were used over three or more independent experimental cultures. iPSC-derived neurons were cultured in BrainPhys Neuronal Media (StemCell) supplemented with 2% B-27 (Gibco), 10 ng/ml BDNF (PeproTech), 10 ng/ml NT-3 (PeproTech), and 1 µg/ml laminin (Corning). 40% of the media was replaced with fresh media twice per week. For Piggybac-delivered NGN2 neurons, 10 µM 5-Fluoro-2′-deoxyuridine and 10 µM uridine were included at the time of plating to prevent survival of mitotic cells. These drugs were removed 24 h after plating. Live imaging experiments were performed 21 days after thawing predifferentiated iPSC-derived neurons (DIV21). On DIV18, iPSC-derived neurons were transfected with Lipofectamine Stem (Thermo Fisher Scientific) and 1–2.5 µg total plasmid DNA. Immunostaining experiments were performed at DIV14. The published protocol can be found on Protocols.io (https://doi.org/10.17504/protocols.io.x54v9dj4zg3e/v1).

Live-cell imaging and motility quantification

iNeurons were imaged on DIV21 in low fluorescence Hibernate A medium (Brain Bits) supplemented with 2% B27, 10 ng/ml BDNF, and 10 ng/ml NT-3. Neurons were imaged in an environmental chamber at 37°C. Recordings of mScarlet-SYP+ vesicles for Figs. 1 and 4 were acquired on a PerkinElmer UltraView Vox Spinning Disk Confocal system with a Nikon Eclipse Ti inverted microscope, using a Plan Apochromat 60× 1.40 NA oil immersion objective and a Hamamatsu EMCCD C9100-50 camera controlled by Volocity software. Following a scheduled microscope upgrade, live imaging for Figs. 2 and 4 was instead

Table 2. **Antibodies**

Antibody	Source	Application/Dilution
Primary antibodies		
Anti-RAB8A (phospho T72), rabbit monoclonal	Abcam (Cat# ab230260, RRID:AB_2814988)	WB @ 1 µg/ml
Anti-MAP2, mouse monoclonal	Sigma-Aldrich (Cat# MAB3418, RRID:AB_94856)	ICC @ 1:200
Anti-synaptophysin, Guinea pig polyclonal	Synaptic Systems (Cat# 101-004, RRID:AB_1210382)	ICC @ 1:500
Anti-synaptophysin, mouse monoclonal	Santa Cruz (Cat# sc-17750, RRID:AB_628311)	WB @ 1:2,000
Anti-Synaptobrevin2 (VAMP2), rabbit monoclonal	Cell Signaling Technology (Cat# 13508, RRID:AB_2798240)	ICC @, WB @ 1:250
Anti-RAB3A, rabbit polyclonal	Proteintech (Cat# 15029-1-AP, RRID:AB_2177378)	WB @ 1:1,000
Anti-golgin-97, rabbit monoclonal	Cell Signaling Technology (Cat# 13192, RRID:AB_2798144)	ICC @ 1:200
Anti-βIII-tubulin	Abcam (Cat# ab7751, RRID:AB_306045)	ICC @ 1:500
Anti-HA, mouse monoclonal	BioLegend (Cat# 901501, RRID:AB_2565006)	WB @ 1:2000
Anti-DENN, rabbit monoclonal	Abcam (Cat# ab134117, RRID:AB_2650580)	WB @ 1:1,000
Anti-GFP, Chicken polyclonal	AvesLabs (Cat# GFP-1020, RRID:AB_10000240)	WB @ 1:5,000
Anti-SNAP-tag, rabbit polyclonal	New England BioLabs (Cat# P9310S, RRID:AB_10631145)	WB @ 1:1,000
Secondary antibodies		
Anti-rabbit IgG-IRDye 800CW, donkey polyclonal	Li-COR Biosciences (Cat# 926-32213, RRID:AB_621848)	WB @ 1:20,000
Anti-rabbit IgG-IRDye 680RD, donkey polyclonal	Li-COR Biosciences (Cat# 926-68073, RRID:AB_10954442)	WB @ 1:20,000
Anti-mouse IgG-IRDye 800CW, donkey polyclonal	Li-COR Biosciences (Cat# 926-32212, RRID:AB_621847)	WB @ 1:20,000
Anti-Chicken IRDye 680RD, donkey polyclonal	Li-COR Biosciences (Cat# 926-68075, RRID: AB_10974977)	WB @ 1:20,000
Anti-rabbit IgG (H+L) alexa fluor 555, goat polyclonal	Thermo Fisher Scientific (Cat# A-32732, RRID: AB_2633281)	ICC @ 1:1,000
Anti-Guinea pig IgG (H+L) alexa fluor 488, goat polyclonal	Thermo Fisher Scientific (Cat# A-11073, RRID: AB_2534117)	ICC @ 1:1,000
Anti-mouse IgG (H+L) alexa fluor 647, goat polyclonal	Thermo Fisher Scientific (Cat# A-32728, RRID:AB_2633277)	ICC @ 1:1,000

performed using a Hamamatsu ORCA-Fusion C14440-20UP camera controlled by VisiView software. Axons were identified based on morphological parameters (Boecker et al., 2020; Kaech and Banker, 2006), and measurements were made to image ~100–150 µm from the neuronal soma. After identifying this region, one photobleaching cycle was performed with the 405 nm laser for 3 ms/pixel using a ViRTEx Realtime Experiment Control Device. All time-lapse recordings were acquired at a frame rate of 5 frames/sec for 5 min. The published protocol can be found on Protocols.io (https://doi.org/10.17504/protocols.io.5jyl8p9mdg2w/v1).

Kymographs of axonal SVPs were generated using the Multiple Kymograph plugin (FIJI). The line width was set to five pixels. For flux quantification, anterograde and retrograde vesicle tracks were manually annotated and counted by a blinded investigator. For anterograde velocity quantification, 10–15 representative anterograde vesicle tracks from each kymograph were traced, and velocity was calculated from the average of their slopes.

Figure legends contain the statistical test used and specific P values for each quantification. RStudio version 2021.9.2.382 was used to perform a linear mixed effects model (LME; R package "nlme"). The genotype (or, in MLi-2 experiments, the treatment condition) was treated as the fixed effect. The independent experiment/culture being recorded was treated as the random effect. For all quantifications, at least three independent experiments were analyzed.

Immunostaining and quantification

At DIV14, human iNeurons were fixed in 4% paraformaldehyde supplemented with 4% sucrose for 15 min, washed four times with PBS, and permeabilized with 0.2% Triton-X in PBS for 15 min. Cells were then blocked for 1 h with 5% goat serum and 1% BSA in PBS. Neurons were then incubated in primary antibody (see Table 2) diluted in blocking solution at room temperature for 1 h, washed three times with PBS, and incubated in secondary antibody (see Table 2) diluted in blocking solution for 1 h at room temperature. After three washes with PBS, coverslips were mounted in ProLong Gold Antifade Mountant (Thermo Fisher Scientific). Images were acquired as z stacks at 200 nm step-size using a spinning disk confocal setup as described above. The published protocol can be found in Protocols.io (https://doi.org/10.17504/protocols.io.8epv5x91ng1b/v1).

For experiments shown in Fig. 3, A–C, the MAP2 channel was used to select an ROI around the somatic compartment by a blinded investigator. This ROI was used to measure the mean grey value of the SYP and SYB2 signals using sum projections. SYP/SYB2 intensity for each neuron was normalized to the average intensity of the WT neurons from that experimental replicate. Figure legends contain the statistical test used and specific P values for each quantification. RStudio version 2021.9.2.382 was used to perform a linear mixed effects model (LME; R package "nlme"). The genotype was treated as the fixed effect. The independent experiment/culture was treated as the random effect. For all quantifications, at least three independent experiments were analyzed.

For experiments shown in Fig. 3, D–G, HEK cells transfected 24 h prior with 6 µl:1 µg mix of FUGENE and pBI-BFP-NL1 (bicistronic vector expressing untagged NL1 and cytosolic BFP) were added to DIV13 iNeurons (100 K transfected HEK cells added to DIV13 iNeurons cultured in 35-mm imaging dishes). 24 h after the addition of transfected HEK cells, at iNeuron DIV14, cells were fixed for immunocytochemistry in 4% paraformaldehyde supplemented with 4% sucrose and stained as described above (see Tables 1 and 2 for antibody information). For analysis, the BFP-NL1 channel was used to select an ROI around an NL1+ HEK cell. To determine SYP and SYB2 intensity within presynaptic regions spanning the NL1+ HEK ROI, max-projection images were created and FIJI's thresholding tool was used to segment an 8-bit object mask based on the top 1% intensity of the SYP or SYB2 channel. FIJI's Analyze Particles tool was then used on the object mask redirected to the original SYP or SYB2 image channel to determine intensity values for individual presynaptic puncta. Figure legends contain the statistical test used and specific P values for each quantification. RStudio version 2021.9.2.382 was used to perform a linear mixed effects model (LME; R package "nlme"). The genotype was treated as the fixed effect. The independent experiment/culture and the field of view were treated as random effects, with the field of view nested within the experiment. For all quantifications, at least three independent experiments were analyzed.

For experiments shown in Fig. S2, E and F, the MAP2 channel was used to select an ROI around the somatic compartment by a blinded investigator. This ROI was used to measure the mean grey value of the somatic SYP signal using a sum projection. The "Adjust Threshold" function in ImageJ was used to create a mask on the region of high-intensity golgin-97 signal, and this ROI was used to measure the mean grey value of the SYP signal colocalized with the TGN. Figure legends contain the statistical test used and specific P values for each quantification. RStudio version 2021.9.2.382 was used to perform a linear mixed effects model (LME; R package "nlme"). The genotype was treated as the fixed effect. The independent experiment/culture was treated as the random effects. For all quantifications, at least three independent experiments were analyzed.

Neuronal lysis and immunoblotting

iNeurons were washed twice with ice-cold PBS and lysed with RIPA buffer (50 mM Tris-HCl, 150 mM NaCl, 0.1% Triton X-100, 0.5% deoxycholate, 0.1% SDS, 2× Halt Protease and Phosphatase inhibitor, 2mg/ml microcystin-LR). Samples were centrifuged for 10 min at 17,000 *g* and protein concentration of the supernatant was determined by BCA assay. Neuronal proteins (SYP, SYB2, and RAB3A) were resolved on 15% acrylamide gels.

Proteins were transferred to Immobilon-FL PVDF membranes (Millipore) using a wet blot transfer system. Membranes were then stained for total protein using LI-COR Revert 700 Total Protein Stain. Following imaging of total protein stain, membranes were de-stained and blocked for 5 min with Bio-Rad EveryBlot blocking buffer. Membranes were incubated with primary antibody diluted in EveryBlot at 4°C overnight. After three washes with TBS (50 mM Tris-HCl [pH 7.4], 274 mM NaCl, 9 mM KCl) with 0.1% Tween-20, membranes were incubated with secondary antibodies diluted in EveryBlot with 0.01% SDS for 1 h at RT. Following three more washes with TBS with 0.1% Tween-20, membranes were imaged using an Odyssey CLx Infrared Imaging System (LI-COR). Western blots were analyzed with Image Studio Software (LI-COR). When necessary, stripping and reprobing were performed using LICOR NewBlot IR stripping buffer according to manufacturer instructions. The published protocol can be found in Protocols.io (https://doi.org/10.17504/protocols.io.5jyl8j5zrg2w/v1).

Cell line culture

HEK293T cells were maintained in DMEM (Corning) with 10% fetal bovine serum (HyClone). Cells were maintained at 37°C in a 5% CO_2 incubator. Cells were tested for mycoplasma contamination routinely using a MycoAlert detection kit (LT07; Lonza). For coimmunoprecipitation experiments, cells were plated on three 10-cm tissue culture dishes per condition and transfected 24 h before lysis using FuGENE 6 (6–12 µg total plasmid DNA; Promega). The published protocol can be found in Protocols.io (https://doi.org/10.17504/protocols.io.kxygx3zeog8j/v1).

Coimmunoprecipitation experiments and quantification

HEK293T cells were lysed 24 h after transfection. For experiments not involving lambda protein phosphatase (λPP), cells were lysed in buffer containing 10 mM Tris-HCl pH 7.5, 150 mM NaCl, and 0.5 mM EDTA, with 0.5% NP-40 and protease inhibitors (1 mM PMSF, 0.01 mg/ml TAME, 0.01 mg/ml leupeptin, 0.001 mg/ml pepstatin A). Lysates were clarified at 10 × *g* at 4°C for 10 min. GFP-Trap Magnetic Particles M-270 were used for experiments involving MADD due to the protein's large size; otherwise, GFP-Trap Magnetic Agarose beads were used. 25 µl of bead slurry per experimental condition were washed twice in wash buffer (10 mM Tris-HCl pH 7.5, 150 mM NaCl, 0.5 mM EDTA; with 0.4% Triton X-100 for MADD pulldowns) for 5 min at 4°C and then equilibrated in lysis buffer for 5 min at 4°C. Beads were incubated with clarified lysate for 1 h at 4°C under rotating agitation. Following incubation, beads were washed three times for 10 min in wash buffer at 4°C and then resuspended in 60 µl denaturing buffer. The beads were then boiled to release the bound proteins.

For experiments using λPP, cells were lysed in 1× NEBuffer for Protein MetalloPhosphatases (New England BioLabs; supplied with λPP) with 0.5% NP-40 and 0.01 mg/ml leupeptin. Lysates were clarified at 10 × *g* at 4°C for 10 min. For conditions with λPP, 60 µl of 10 mM $MnCl_2$ and 24 µl λPP (2,400 units) were added to clarified lysate for a final reaction volume of 600 µl and incubated at 30°C for 30 min. The same was performed for λPP-negative conditions, with 24 µl ddH_2O instead. After incubation with λPP, incubation with beads was performed as described above. Published protocol can be found in Protocols.io (https://doi.org/10.17504/protocols.io.6qpvr36o2vmk/v1).

Coimmunoprecipitation was analyzed by Western blot (see "Immunoblotting"). Proteins from the same experiment were processed in parallel and resolved on different acrylamide gels based on protein size: 6% for HA-MADD; 10% for RAB3GAP2, RAB-GDI1, and SNAP-Synapsin; and 12% for EGFP-RAB3A, pT RAB, EGFP vector, and HA-RIM2. Figure legends contain the

statistical test used and specific P values for each quantification. For quantifications, the residual signal caused by non-specific binding was subtracted, relative to the amount of GFP+ bait in each lane. Specific calculations for each lane can be found in the dataset accessible on Zenodo.

Online supplemental material

Supplemental data and legends relating to Figs. 1, 3, and 5 can be found in Figs. S1, S2, S3, and S4. Fig. S5 includes AlphaFold and AlphaFold-Multimer predictions relating to Figs. 4 and 5.

Data availability

Primary data that are presented in this study have been deposited in a Zenodo repository and are publicly available as of the date of publication. These can be accessed using the Digital Object Identifier https://doi.org/10.5281/zenodo.8156733. Any additional information required to reanalyze the data reported in this paper is available from the lead contact upon request.

Lead contact

Further information and requests for resources and reagents should be directed to and will be fulfilled by the lead contact, Erika L.F. Holzbaur (holzbaur@pennmedicine.edu).

Acknowledgments

We thank Mariko Tokito for assistance in the cloning of plasmid constructs. We thank Michael Ward (National Institutes of Health), Erika Lara Flores (National Institutes of Health), and Bill Skarnes (The Jackson Laboratory) for their expertise in utilizing resources from the iPSC Neurodegeneration Initiative (iNDI). Cartoon schematics were created in part with http://BioRender.com. Protein structures in Fig. 2 were supplied from http://UniProt.org under the Creative Commons Attribution 4.0 International (CC BY 4.0) License (PDB: 7LHT for LRRK2, 7L4J for PPM1H). AlphaFold and AlphaFold-Multimer (accessed through COSMIC² Gateway) were used for structural models and are cited in the main text. *PPM1H* KO iPSCs used in this study were previously generated by C. Alexander Boecker (Dou et al., 2023). Source plasmid DNA for HA-RIM2 was a gift from Ruben Bierings (Erasmus University Medical Center). We thank C. Alexander Boecker, Juliet Goldsmith, and Elizabeth Gallagher for helpful insights and discussions.

This work was supported by the National Institutes of Health (1 F31 NS124249-01 and T32-AG-000255 to D. Dou, F32 NS117672 to J. Aiken, and R35 GM126950 to E.L.F. Holzbaur) and the Michael J. Fox Foundation (MJFF) (MJFF-021130, MJFF-15100, and MJFF-019411 to E.L.F. Holzbaur). The E.L.F. Holzbaur laboratory is funded by the joint efforts of The MJFF and the Aligning Science Across Parkinson's initiative. MJFF administers the grant ASAP-000350 on behalf of ASAP and itself.

Author contributions: Conceptualization, D. Dou, J. Aiken, and E.L.F. Holzbaur; methodology, D. Dou and J. Aiken; investigation, D. Dou and J. Aiken; writing—original draft, D. Dou, J. Aiken, and E.L.F. Holzbaur; writing—review and editing, D. Dou, J. Aiken, and E.L.F. Holzbaur; funding acquisition, D. Dou, J. Aiken, and E.L.F. Holzbaur; supervision, E.L.F. Holzbaur.

Disclosures: The authors declare no competing interests exist.

Submitted: 19 July 2023
Revised: 1 February 2024
Accepted: 4 March 2024

References

Aiken, J., and E.L.F. Holzbaur. 2024. Spastin locally amplifies microtubule dynamics to pattern the axon for presynaptic cargo delivery. *Curr. Biol.* In press.

Behesti, H., T.R. Fore, P. Wu, Z. Horn, M. Leppert, C. Hull, and M.E. Hatten. 2018. ASTN2 modulates synaptic strength by trafficking and degradation of surface proteins. *Proc. Natl. Acad. Sci. USA.* 115:E9717–E9726. https://doi.org/10.1073/pnas.1809382115

Bendor, J., T. Logan, and R.H. Edwards. 2013. The function of α-synuclein. *Neuron.* 79:1044–1066. https://doi.org/10.1016/j.neuron.2013.09.004

Berndsen, K., P. Lis, W.M. Yeshaw, P.S. Wawro, R.S. Nirujogi, M. Wightman, T. Macartney, M. Dorward, A. Knebel, F. Tonelli, et al. 2019. PPM1H phosphatase counteracts LRRK2 signaling by selectively dephosphorylating Rab proteins. *Elife.* 8:e50416. https://doi.org/10.7554/eLife.50416

Bieri, G., M. Brahic, L. Bousset, J. Couthouis, N.J. Kramer, R. Ma, L. Nakayama, M. Monbureau, E. Defensor, B. Schüle, et al. 2019. LRRK2 modifies α-syn pathology and spread in mouse models and human neurons. *Acta Neuropathol.* 137:961–980. https://doi.org/10.1007/s00401-019-01995-0

Boecker, C.A., M.A. Olenick, E.R. Gallagher, M.E. Ward, and E.L.F. Holzbaur. 2020. ToolBox: Live Imaging of intracellular organelle transport in induced pluripotent stem cell-derived neurons. *Traffic.* 21:138–155. https://doi.org/10.1111/tra.12701

Boecker, C.A., J. Goldsmith, D. Dou, G.G. Cajka, and E.L.F. Holzbaur. 2021. Increased LRRK2 kinase activity alters neuronal autophagy by disrupting the axonal transport of autophagosomes. *Curr. Biol.* 31:2140–2154.e6. https://doi.org/10.1016/j.cub.2021.02.061

Bonanomi, D., F. Benfenati, and F. Valtorta. 2006. Protein sorting in the synaptic vesicle life cycle. *Prog. Neurobiol.* 80:177–217. https://doi.org/10.1016/j.pneurobio.2006.09.002

Bonet-Ponce, L., A. Beilina, C.D. Williamson, E. Lindberg, J.H. Kluss, S. Saez-Atienzar, N. Landeck, R. Kumaran, A. Mamais, C.K.E. Bleck, et al. 2020. LRRK2 mediates tubulation and vesicle sorting from lysosomes. *Sci. Adv.* 6:eabb2454. https://doi.org/10.1126/sciadv.abb2454

Brown, T.L., and P.H. Howe. 1998. MADD is highly homologous to a Rab3 guanine-nucleotide exchange protein (Rab3-GEP). *Curr. Biol.* 8:R191. https://doi.org/10.1016/S0960-9822(98)70121-6

Brzozowski, C.F., B.A. Hijaz, V. Singh, N.Z. Gcwensa, K. Kelly, E.S. Boyden, A.B. West, D. Sarkar, and L.A. Volpicelli-Daley. 2021. Inhibition of LRRK2 kinase activity promotes anterograde axonal transport and presynaptic targeting of α-synuclein. *Acta Neuropathol. Commun.* 9:180. https://doi.org/10.1186/s40478-021-01283-7

Cianfrocco, M., M. Wong, and C. Youn. 2017a. COSMIC2—A science gateway for cryo-electron microscopy. https://doi.org/10.6084/m9.figshare.5481430.v1

Cianfrocco, M.A., M. Wong-Barnum, C. Youn, R. Wagner, and A. Leschziner. 2017b. COSMIC2: A science gateway for cryo-electron microscopy structure determination. *In* Proceedings of the Practice and Experience in Advanced Research Computing 2017 on Sustainability, Success and Impact. Association for Computing Machinery, New York, NY. 1–5. https://doi.org/10.1145/3093338.3093390

Cirnaru, M.D., A. Marte, E. Belluzzi, I. Russo, M. Gabrielli, F. Longo, L. Arcuri, L. Murru, L. Bubacco, M. Matteoli, et al. 2014. LRRK2 kinase activity regulates synaptic vesicle trafficking and neurotransmitter release through modulation of LRRK2 macro-molecular complex. *Front. Mol. Neurosci.* 7:49. https://doi.org/10.3389/fnmol.2014.00049

De Pace, R., D.J. Britt, J. Mercurio, A.M. Foster, L. Djavaherian, V. Hoffmann, D. Abebe, and J.S. Bonifacino. 2020. Synaptic vesicle precursors and lysosomes are transported by different mechanisms in the axon of mammalian neurons. *Cell Rep.* 31:107775. https://doi.org/10.1016/j.celrep.2020.107775

Domingo, A., and C. Klein. 2018. Genetics of Parkinson disease. *In* Handbook of Clinical Neurology. Vol. 147. Elsevier, Amsterdam, The Netherlands. 211–227. https://doi.org/10.1016/B978-0-444-63233-3.00014-2

Dong, J., M. Chen, J.R.T. van Weering, K.W. Li, A.B. Smit, R.F. Toonen, and M. Verhage. 2024. Rab10 regulates neuropeptide release by maintaining Ca^{2+} homeostasis and protein synthesis. *bioRxiv*. https://doi.org/10.1101/2024.01.02.573873 (Preprint posted January 02, 2024).

Dou, D., E.M. Smith, C.S. Evans, C.A. Boecker, and E.L.F. Holzbaur. 2023. Regulatory imbalance between LRRK2 kinase, PPM1H phosphatase, and ARF6 GTPase disrupts the axonal transport of autophagosomes. *Cell Rep.* 42:112448. https://doi.org/10.1016/j.celrep.2023.112448

Evans, R., M. O'Neill, A. Pritzel, N. Antropova, A. Senior, T. Green, A. Žídek, R. Bates, S. Blackwell, J. Yim, et al. 2022. Protein complex prediction with AlphaFold-Multimer. *bioRxiv*. https://doi.org/10.1101/2021.10.04.463034 (Preprint posted March 10, 2022).

Fell, M.J., C. Mirescu, K. Basu, B. Cheewatrakoolpong, D.E. DeMong, J.M. Ellis, L.A. Hyde, Y. Lin, C.G. Markgraf, H. Mei, et al. 2015. MLi-2, a potent, selective, and centrally active compound for exploring the therapeutic potential and safety of LRRK2 kinase inhibition. *J. Pharmacol. Exp. Ther.* 355:397–409. https://doi.org/10.1124/jpet.115.227587

Fernandopulle, M.S., R. Prestil, C. Grunseich, C. Wang, L. Gan, and M.E. Ward. 2018. Transcription factor-mediated differentiation of human iPSCs into neurons. *Curr. Protoc. Cell Biol.* 79:e51. https://doi.org/10.1002/cpcb.51

Fischer von Mollard, G., G.A. Mignery, M. Baumert, M.S. Perin, T.J. Hanson, P.M. Burger, R. Jahn, and T.C. Südhof. 1990. rab3 is a small GTP-binding protein exclusively localized to synaptic vesicles. *Proc. Natl. Acad. Sci. USA*. 87:1988–1992. https://doi.org/10.1073/pnas.87.5.1988

Fonseca-Ornelas, L., J.M.S. Stricker, S. Soriano-Cruz, B. Weykopf, U. Dettmer, C.R. Muratore, C.R. Scherzer, and D.J. Selkoe. 2022. Parkinson-causing mutations in LRRK2 impair the physiological tetramerization of endogenous α-synuclein in human neurons. *NPJ Parkinsons Dis.* 8:118. https://doi.org/10.1038/s41531-022-00380-1

Giovedì, S., P. Vaccaro, F. Valtorta, F. Darchen, P. Greengard, G. Cesareni, and F. Benfenati. 2004. Synapsin is a novel Rab3 effector protein on small synaptic vesicles. I. Identification and characterization of the synapsin I-Rab3 interactions in vitro and in intact nerve terminals. *J. Biol. Chem.* 279:43760–43768. https://doi.org/10.1074/jbc.M403293200

Goldsmith, J., A. Ordureau, J.W. Harper, and E.L.F. Holzbaur. 2022. Brain-derived autophagosome profiling reveals the engulfment of nucleoid-enriched mitochondrial fragments by basal autophagy in neurons. *Neuron*. 110:967–976.e8. https://doi.org/10.1016/j.neuron.2021.12.029

Goldstein, A.Y., X. Wang, and T.L. Schwarz. 2008. Axonal transport and the delivery of pre-synaptic components. *Curr. Opin. Neurobiol.* 18:495–503. https://doi.org/10.1016/j.conb.2008.10.003

Gomez, R.C., P. Wawro, P. Lis, D.R. Alessi, and S.R. Pfeffer. 2019. Membrane association but not identity is required for LRRK2 activation and phosphorylation of Rab GTPases. *J. Cell Biol.* 218:4157–4170. https://doi.org/10.1083/jcb.201902184

Gracia-Diaz, C., J.E. Perdomo, M.E. Khan, B. Disanza, G.G. Cajka, S. Lei, A. Gagne, J.A. Maguire, T. Roule, O. Shalem, et al. 2023. High density SNP array and reanalysis of genome sequencing uncovers CNVs associated with neurodevelopmental disorders in KOLF2.1J iPSCs. *bioRxiv*. https://doi.org/10.1101/2023.06.26.546614 (Preprint posted June 26, 2023).

Guedes-Dias, P., J.J. Nirschl, N. Abreu, M.K. Tokito, C. Janke, M.M. Magiera, and E.L.F. Holzbaur. 2019. Kinesin-3 responds to local microtubule dynamics to target synaptic cargo delivery to the presynapse. *Curr. Biol.* 29:268–282.e8. https://doi.org/10.1016/j.cub.2018.11.065

Hannah, M.J., A.A. Schmidt, and W.B. Huttner. 1999. Synaptic vesicle biogenesis. *Annu. Rev. Cell Dev. Biol.* 15:733–798. https://doi.org/10.1146/annurev.cellbio.15.1.733

Haugarvoll, K., R. Rademakers, J.M. Kachergus, K. Nuytemans, O.A. Ross, J.M. Gibson, E.-K. Tan, C. Gaig, E. Tolosa, S. Goldwurm, et al. 2008. Lrrk2 R1441C parkinsonism is clinically similar to sporadic Parkinson disease. *Neurology*. 70:1456–1460. https://doi.org/10.1212/01.wnl.0000304044.22253.03

Healy, D.G., M. Falchi, S.S. O'Sullivan, V. Bonifati, A. Durr, S. Bressman, A. Brice, J. Aasly, C.P. Zabetian, S. Goldwurm, et al. 2008. Phenotype, genotype, and worldwide genetic penetrance of LRRK2-associated Parkinson's disease: A case-control study. *Lancet Neurol.* 7:583–590. https://doi.org/10.1016/S1474-4422(08)70117-0

Hoopmann, P., A. Punge, S.V. Barysch, V. Westphal, J. Bückers, F. Opazo, I. Bethani, M.A. Lauterbach, S.W. Hell, and S.O. Rizzoli. 2010. Endosomal sorting of readily releasable synaptic vesicles. *Proc. Natl. Acad. Sci. USA*. 107:19055–19060. https://doi.org/10.1073/pnas.1007037107

Huang, C.C., D.M. Yang, C.C. Lin, and L.S. Kao. 2011. Involvement of Rab3A in vesicle priming during exocytosis: Interaction with munc13-1 and munc18-1. *Traffic*. 12:1356–1370. https://doi.org/10.1111/j.1600-0854.2011.01237.x

Hummel, J.J.A., and C.C. Hoogenraad. 2021. Specific KIF1A-adaptor interactions control selective cargo recognition. *J. Cell Biol.* 220:e202105011. https://doi.org/10.1083/jcb.202105011

Islam, M.S., H. Nolte, W. Jacob, A.B. Ziegler, S. Pütz, Y. Grosjean, K. Szczepanowska, A. Trifunovic, T. Braun, H. Heumann, et al. 2016. Human R1441C LRRK2 regulates the synaptic vesicle proteome and phosphoproteome in a Drosophila model of Parkinson's disease. *Hum. Mol. Genet.* 25:5365–5382. https://doi.org/10.1093/hmg/ddw352

Jumper, J., R. Evans, A. Pritzel, T. Green, M. Figurnov, O. Ronneberger, K. Tunyasuvunakool, R. Bates, A. Žídek, A. Potapenko, et al. 2021. Highly accurate protein structure prediction with AlphaFold. *Nature*. 596:583–589. https://doi.org/10.1038/s41586-021-03819-2

Kaech, S., and G. Banker. 2006. Culturing hippocampal neurons. *Nat. Protoc.* 1:2406–2415. https://doi.org/10.1038/nprot.2006.356

Kalia, L.V., and A.E. Lang. 2015. Parkinson's disease. *Lancet*. 386:896–912. https://doi.org/10.1016/S0140-6736(14)61393-3

Kalogeropulou, A.F., E. Purlyte, F. Tonelli, S.M. Lange, M. Wightman, A.R. Prescott, S. Padmanabhan, E. Sammler, and D.R. Alessi. 2022. Impact of 100 LRRK2 variants linked to Parkinson's disease on kinase activity and microtubule binding. *Biochem. J.* 479:1759–1783. https://doi.org/10.1042/BCJ20220161

Kat, M., P.E. Bürgisser, H. Janssen, I.M. De Cuyper, I.L. Conte, A.N. Hume, T. Carter, J. Voorberg, C. Margadant, and R. Bierings. 2021. GDP/GTP exchange factor MADD drives activation and recruitment of secretory Rab GTPases to Weibel-Palade bodies. *Blood Adv.* 5:5116–5127. https://doi.org/10.1182/bloodadvances.2021004827

Klein, C., and A. Westenberger. 2012. Genetics of Parkinson's disease. *Cold Spring Harb. Perspect. Med.* 2:a008888. https://doi.org/10.1101/cshperspect.a008888

Kluss, J.H., L. Bonet-Ponce, P.A. Lewis, and M.R. Cookson. 2022. Directing LRRK2 to membranes of the endolysosomal pathway triggers RAB phosphorylation and JIP4 recruitment. *Neurobiol. Dis.* 170:105769. https://doi.org/10.1016/j.nbd.2022.105769

Liu, Z., N. Bryant, R. Kumaran, A. Beilina, A. Abeliovich, M.R. Cookson, and A.B. West. 2018. LRRK2 phosphorylates membrane-bound Rabs and is activated by GTP-bound Rab7L1 to promote recruitment to the trans-Golgi network. *Hum. Mol. Genet.* 27:385–395. https://doi.org/10.1093/hmg/ddx410

Mamais, A., J.H. Kluss, L. Bonet-Ponce, N. Landeck, R.G. Langston, N. Smith, A. Beilina, A. Kaganovich, M.C. Ghosh, L. Pellegrini, et al. 2021. Mutations in LRRK2 linked to Parkinson disease sequester Rab8a to damaged lysosomes and regulate transferrin-mediated iron uptake in microglia. *PLoS Biol.* 19:e3001480. https://doi.org/10.1371/journal.pbio.3001480

Marte, A., I. Russo, C. Rebosio, P. Valente, E. Belluzzi, F. Pischedda, C. Montani, C. Lavarello, A. Petretto, E. Fedele, et al. 2019. Leucine-rich repeat kinase 2 phosphorylation on synapsin I regulates glutamate release at pre-synaptic sites. *J. Neurochem.* 150:264–281. https://doi.org/10.1111/jnc.14778

Matta, S., K. Van Kolen, R. da Cunha, G. van den Bogaart, W. Mandemakers, K. Miskiewicz, P.-J. De Bock, V.A. Morais, S. Vilain, D. Haddad, et al. 2012. LRRK2 controls an EndoA phosphorylation cycle in synaptic endocytosis. *Neuron*. 75:1008–1021. https://doi.org/10.1016/j.neuron.2012.08.022

Meixner, A., K. Boldt, M. Van Troys, M. Askenazi, C.J. Gloeckner, M. Bauer, J.A. Marto, C. Ampe, N. Kinkl, and M. Ueffing. 2011. A QUICK screen for Lrrk2 interaction partners--leucine-rich repeat kinase 2 is involved in actin cytoskeleton dynamics. *Mol. Cell. Proteomics*. 10:M110.001172. https://doi.org/10.1074/mcp.M110.001172

Mundigl, O., M. Matteoli, L. Daniell, A. Thomas-Reetz, A. Metcalf, R. Jahn, and P. De Camilli. 1993. Synaptic vesicle proteins and early endosomes in cultured hippocampal neurons: Differential effects of brefeldin A in axon and dendrites. *J. Cell Biol.* 122:1207–1221. https://doi.org/10.1083/jcb.122.6.1207

Nakata, T., S. Terada, and N. Hirokawa. 1998. Visualization of the dynamics of synaptic vesicle and plasma membrane proteins in living axons. *J. Cell Biol.* 140:659–674. https://doi.org/10.1083/jcb.140.3.659

Nguyen, M., and D. Krainc. 2018. LRRK2 phosphorylation of auxilin mediates synaptic defects in dopaminergic neurons from patients with Parkinson's disease. *Proc. Natl. Acad. Sci. USA*. 115:5576–5581. https://doi.org/10.1073/pnas.1717590115

Niwa, S., Y. Tanaka, and N. Hirokawa. 2008. KIF1Bbeta- and KIF1A-mediated axonal transport of presynaptic regulator Rab3 occurs in a GTP-

dependent manner through DENN/MADD. *Nat. Cell Biol.* 10:1269–1279. https://doi.org/10.1038/ncb1785
Niwa, S., L. Tao, S.Y. Lu, G.M. Liew, W. Feng, M.V. Nachury, and K. Shen. 2017. BORC regulates the axonal transport of synaptic vesicle precursors by activating ARL-8. *Curr. Biol.* 27:2569–2578.e4. https://doi.org/10.1016/j.cub.2017.07.013
Pal, P., M. Taylor, P.Y. Lam, F. Tonelli, C.A. Hecht, P. Lis, R.S. Nirujogi, T.K. Phung, W.M. Yeshaw, E. Jaimon, et al. 2023. Parkinson's VPS35[D620N] mutation induces LRRK2-mediated lysosomal association of RILPL1 and TMEM55B. *Sci Adv.* 9:eadj1205. https://doi.org/10.1126/sciadv.adj1205
Pantazis, C.B., A. Yang, E. Lara, J.A. McDonough, C. Blauwendraat, L. Peng, H. Oguro, J. Kanaujiya, J. Zou, D. Sebesta, et al. 2022. A reference human induced pluripotent stem cell line for large-scale collaborative studies. *Cell Stem Cell.* 29:1685–1702.e22. https://doi.org/10.1016/j.stem.2022.11.004
Persoon, C.M., R.I. Hoogstraaten, J.P. Nassal, J.R.T. van Weering, P.S. Kaeser, R.F. Toonen, and M. Verhage. 2019. The RAB3-RIM pathway is essential for the release of neuromodulators. *Neuron.* 104:1065–1080.e12. https://doi.org/10.1016/j.neuron.2019.09.015
Pfeffer, S.R. 2005. Structural clues to Rab GTPase functional diversity. *J. Biol. Chem.* 280:15485–15488. https://doi.org/10.1074/jbc.R500003200
Pfeffer, S.R. 2013. Rab GTPase regulation of membrane identity. *Curr. Opin. Cell Biol.* 25:414–419. https://doi.org/10.1016/j.ceb.2013.04.002
Pfeffer, S.R. 2017. Rab GTPases: Master regulators that establish the secretory and endocytic pathways. *Mol. Biol. Cell.* 28:712–715. https://doi.org/10.1091/mbc.e16-10-0737
Pfeffer, S.R. 2023. LRRK2 phosphorylation of Rab GTPases in Parkinson's disease. *FEBS Lett.* 597:811–818. https://doi.org/10.1002/1873-3468.14492
Piccoli, G., S.B. Condliffe, M. Bauer, F. Giesert, K. Boldt, S. De Astis, A. Meixner, H. Sarioglu, D.M. Vogt-Weisenhorn, W. Wurst, et al. 2011. LRRK2 controls synaptic vesicle storage and mobilization within the recycling pool. *J. Neurosci.* 31:2225–2237. https://doi.org/10.1523/JNEUROSCI.3730-10.2011
Piccoli, G., F. Onofri, M.D. Cirnaru, C.J.O. Kaiser, P. Jagtap, A. Kastenmüller, F. Pischedda, A. Marte, F. von Zweydorf, A. Vogt, et al. 2014. Leucine-rich repeat kinase 2 binds to neuronal vesicles through protein interactions mediated by its C-terminal WD40 domain. *Mol. Cell. Biol.* 34:2147–2161. https://doi.org/10.1128/MCB.00914-13
Pischedda, F., and G. Piccoli. 2021. LRRK2 at the pre-synaptic site: A 16-years perspective. *J. Neurochem.* 157:297–311. https://doi.org/10.1111/jnc.15240
Prado, V.F., and M.A.M. Prado. 2002. Signals involved in targeting membrane proteins to synaptic vesicles. *Cell. Mol. Neurobiol.* 22:565–577. https://doi.org/10.1023/a:1021884319363
Ramos, D.M., W.C. Skarnes, A.B. Singleton, M.R. Cookson, and M.E. Ward. 2021. Tackling neurodegenerative diseases with genomic engineering: A new stem cell initiative from the NIH. *Neuron.* 109:1080–1083. https://doi.org/10.1016/j.neuron.2021.03.022
Ruiz-Martínez, J., A. Gorostidi, B. Ibañez, A. Alzualde, D. Otaegui, F. Moreno, A. López de Munain, A. Bergareche, J.C. Gómez-Esteban, and J.F. Martí Massó. 2010. Penetrance in Parkinson's disease related to the LRRK2 R1441G mutation in the Basque country (Spain). *Mov. Disord.* 25:2340–2345. https://doi.org/10.1002/mds.23278
Ryan, M., J.A. McDonough, M.E. Ward, M.R. Cookson, W.C. Skarnes, and F.T. Merkle. 2024. Large structural variants in KOLF2.1J are unlikely to compromise neurological disease modelling. *bioRxiv.* https://doi.org/10.1101/2024.01.29.577739 (Preprint posted January 29, 2024).
Schlüter, O.M., M. Khvotchev, R. Jahn, and T.C. Südhof. 2002. Localization versus function of Rab3 proteins. Evidence for a common regulatory role in controlling fusion. *J. Biol. Chem.* 277:40919–40929. https://doi.org/10.1074/jbc.M203704200
Schlüter, O.M., F. Schmitz, R. Jahn, C. Rosenmund, and T.C. Südhof. 2004. A complete genetic analysis of neuronal Rab3 function. *J. Neurosci.* 24:6629–6637. https://doi.org/10.1523/JNEUROSCI.1610-04.2004
Schlüter, O.M., J. Basu, T.C. Südhof, and C. Rosenmund. 2006. Rab3 superprimes synaptic vesicles for release: Implications for short-term synaptic plasticity. *J. Neurosci.* 26:1239–1246. https://doi.org/10.1523/JNEUROSCI.3553-05.2006
Sheehan, P., M. Zhu, A. Beskow, C. Vollmer, and C.L. Waites. 2016. Activity-dependent degradation of synaptic vesicle proteins requires Rab35 and the ESCRT pathway. *J. Neurosci.* 36:8668–8686. https://doi.org/10.1523/JNEUROSCI.0725-16.2016
Shimizu, H., S. Kawamura, and K. Ozaki. 2003. An essential role of Rab5 in uniformity of synaptic vesicle size. *J. Cell Sci.* 116:3583–3590. https://doi.org/10.1242/jcs.00676
Singh, V., M.A. Menard, G.E. Serrano, T.G. Beach, H.T. Zhao, A. Riley-Di-Paolo, N. Subrahmanian, M.J. LaVoie, and L.A. Volpicelli-Daley. 2023. Cellular and subcellular localization of Rab10 and phospho-T73 Rab10 in the mouse and human brain. *Acta Neuropathol. Commun.* 11:201. https://doi.org/10.1186/s40478-023-01704-9
Stafa, K., E. Tsika, R. Moser, A. Musso, L. Glauser, A. Jones, S. Biskup, Y. Xiong, R. Bandopadhyay, V.L. Dawson, et al. 2014. Functional interaction of Parkinson's disease-associated LRRK2 with members of the dynamin GTPase superfamily. *Hum. Mol. Genet.* 23:2055–2077. https://doi.org/10.1093/hmg/ddt600
Steger, M., F. Tonelli, G. Ito, P. Davies, M. Trost, M. Vetter, S. Wachter, E. Lorentzen, G. Duddy, S. Wilson, et al. 2016. Phosphoproteomics reveals that Parkinson's disease kinase LRRK2 regulates a subset of Rab GTPases. *Elife.* 5:e12813. https://doi.org/10.7554/eLife.12813
Steger, M., F. Diez, H.S. Dhekne, P. Lis, R.S. Nirujogi, O. Karayel, F. Tonelli, T.N. Martinez, E. Lorentzen, S.R. Pfeffer, et al. 2017. Systematic proteomic analysis of LRRK2-mediated Rab GTPase phosphorylation establishes a connection to ciliogenesis. *Elife.* 6:e31012. https://doi.org/10.7554/eLife.31012
Südhof, T.C. 1997. Function of Rab3 GDP-GTP exchange. *Neuron.* 18:519–522. https://doi.org/10.1016/S0896-6273(00)80292-5
Truckenbrodt, S., A. Viplav, S. Jähne, A. Vogts, A. Denker, H. Wildhagen, E.F. Fornasiero, and S.O. Rizzoli. 2018. Newly produced synaptic vesicle proteins are preferentially used in synaptic transmission. *EMBO J.* 37:e98044. https://doi.org/10.15252/embj.201798044
Uytterhoeven, V., S. Kuenen, J. Kasprowicz, K. Miskiewicz, and P. Verstreken. 2011. Loss of skywalker reveals synaptic endosomes as sorting stations for synaptic vesicle proteins. *Cell.* 145:117–132. https://doi.org/10.1016/j.cell.2011.02.039
van Weering, J.R.T., R.F. Toonen, and M. Verhage. 2007. The role of Rab3a in secretory vesicle docking requires association/dissociation of guanidine phosphates and Munc18-1. *PLoS One.* 2:e616. https://doi.org/10.1371/journal.pone.0000616
Varadi, M., S. Anyango, M. Deshpande, S. Nair, C. Natassia, G. Yordanova, D. Yuan, O. Stroe, G. Wood, A. Laydon, et al. 2022. AlphaFold protein structure database: Massively expanding the structural coverage of protein-sequence space with high-accuracy models. *Nucleic Acids Res.* 50:D439–D444. https://doi.org/10.1093/nar/gkab1061
Waschbüsch, D., E. Purlyte, P. Pal, E. McGrath, D.R. Alessi, and A.R. Khan. 2020. Structural basis for Rab8a recruitment of RILPL2 via LRRK2 phosphorylation of switch 2. *Structure.* 28:406–417.e6. https://doi.org/10.1016/j.str.2020.01.005
Wucherpfennig, T., M. Wilsch-Bräuninger, and M. González-Gaitán. 2003. Role of Drosophila Rab5 during endosomal trafficking at the synapse and evoked neurotransmitter release. *J. Cell Biol.* 161:609–624. https://doi.org/10.1083/jcb.200211087
Yeshaw, W.M., A. Adhikari, C.Y. Chiang, H.S. Dhekne, P.S. Wawro, and S.R. Pfeffer. 2023. Localization of PPM1H phosphatase tunes Parkinson's disease-linked LRRK2 kinase-mediated Rab GTPase phosphorylation and ciliogenesis. *Proc. Natl. Acad. Sci. USA.* 120:e2315171120. https://doi.org/10.1073/pnas.2315171120
Yun, H.J., J. Park, D.H. Ho, H. Kim, C.-H. Kim, H. Oh, I. Ga, H. Seo, S. Chang, I. Son, and W. Seol. 2013. LRRK2 phosphorylates Snapin and inhibits interaction of Snapin with SNAP-25. *Exp. Mol. Med.* 45:e36. https://doi.org/10.1038/emm.2013.68

Supplemental material

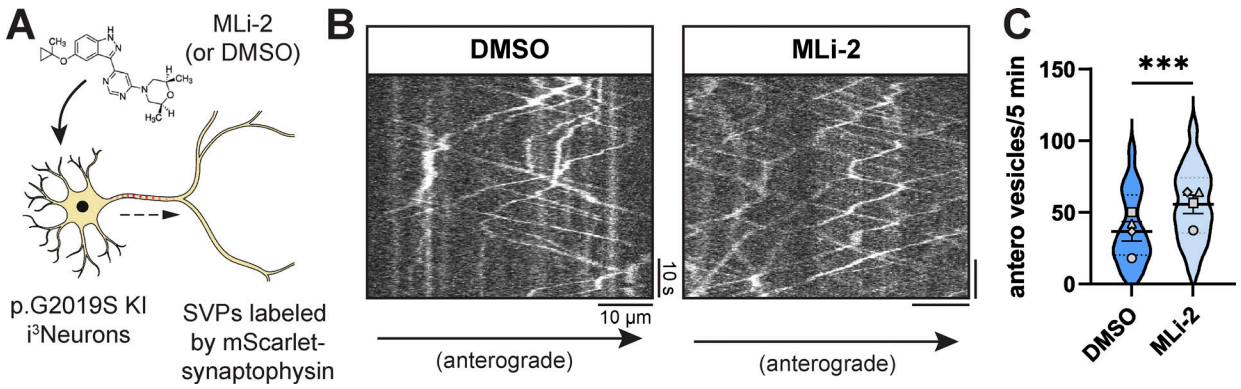

Figure S1. **Related to** Fig. 1**. (A)** Cartoon depicting p.G2019S KI i^{3}Neuron treated overnight with DMSO or 100 nM MLi-2. **(B)** Kymographs of axonal mScarlet-SYP+ vesicles in p.G2019S KI i^{3}Neurons treated with DMSO or MLi-2. **(C)** Anterograde flux of SYP+ vesicles in p.G2019S KI i^{3}Neurons treated with DMSO or MLi-2 (n = 39–41 neurons from four independent experiments; ***P < 0.001; linear mixed effects model). Scatter plot points indicate the means of four independent experiments, and error bars show mean ± SD of these points.

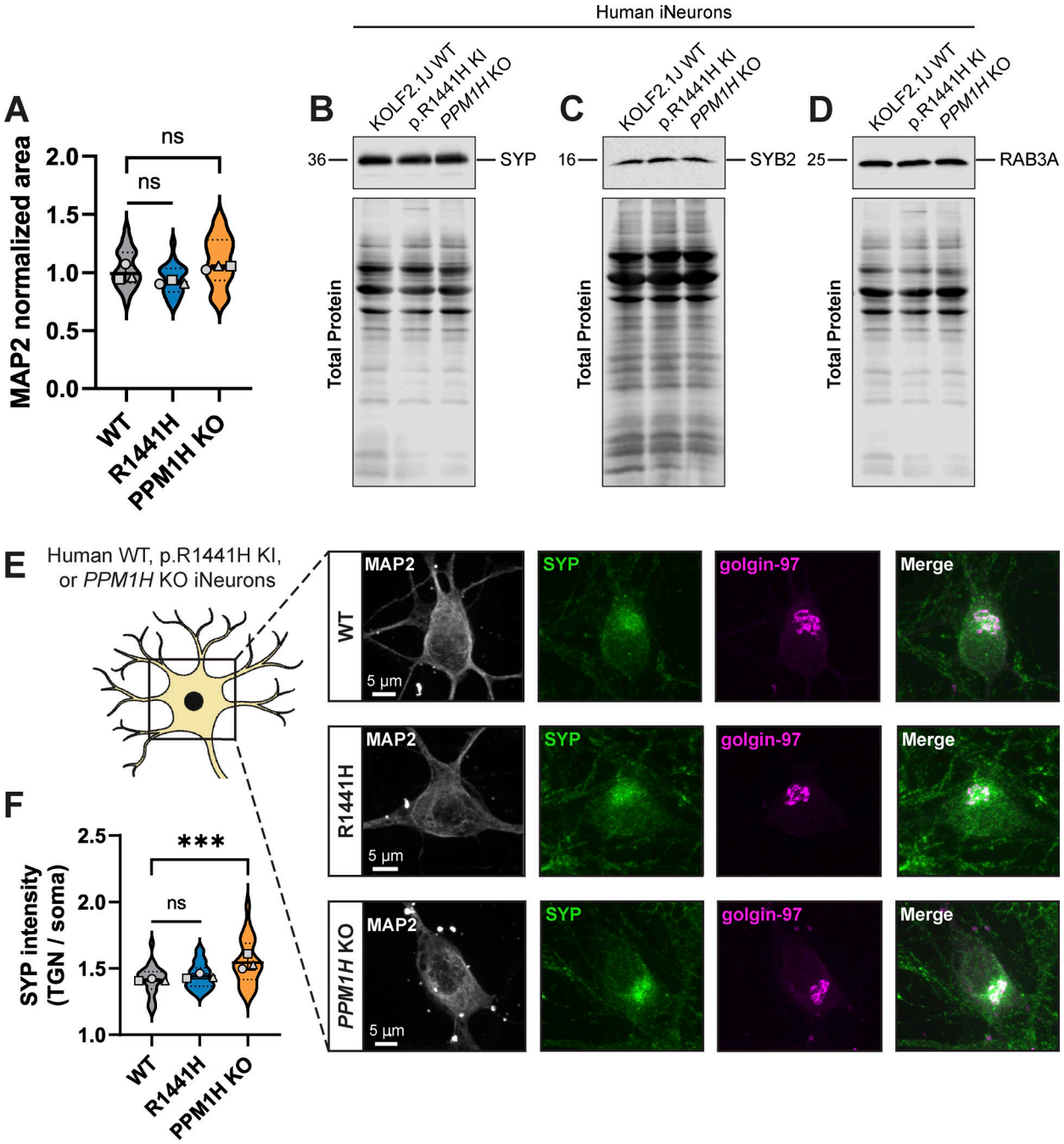

Figure S2. **Related to** Fig. 3. **(A)** Normalized somal MAP2 area of WT, p.R1441H KI, and *PPM1H* KO iNeurons for dataset shown in Fig. 3, A–C (n = 24 neurons from three independent experiments; ns > 0.0540; linear mixed effects model). **(B–D)** Example total protein stain and immunoblot of SYP (B), SYB2 (C), and RAB3A (D) in DIV21 WT, p.R1441H KI, and *PPM1H* KO iNeurons. **(E)** Representative images of DIV14 WT, p.R1441H KI, and *PPM1H* KO iNeuron somas, stained for endogenous MAP2, SYP, and golgin-97. **(F)** Ratio of SYP intensity (mean gray value) colocalized with golgin-97 signal/SYP intensity (mean gray value) of whole soma, in WT, p.R1441H KI, and *PPM1H* KO iNeurons (n = 24 neurons from three independent experiments; ns = 0.4638; ***P < 0.001; linear mixed effects model). Scatter plot points indicate the means of three independent experiments, and error bars show the mean ± SD of these points. Source data are available for this figure: SourceData FS2.

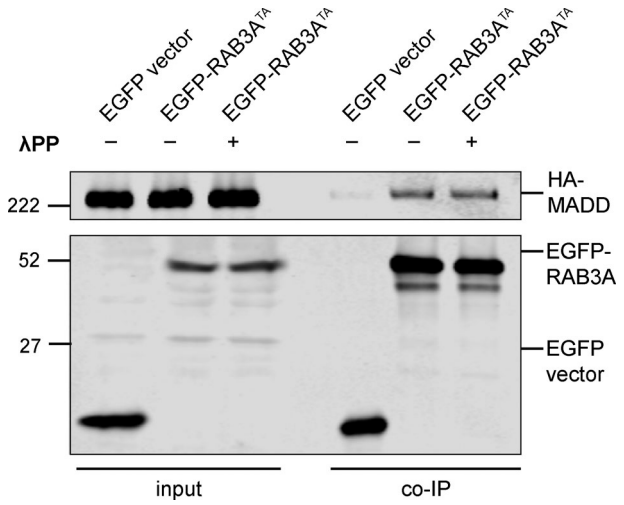

Figure S3. **Related to** Fig. 4**.** Immunoblot of MADD coimmunoprecipitation by RAB3A^{TA}, coexpressed in HEK293T cells, with or without 30 min treatment of lysate with lambda protein phosphatase (λPP; 200 units λPP per 50 µl reaction volume). For co-IP experiment shown, samples were processed and immunoblotted in parallel. Source data are available for this figure: SourceData FS3.

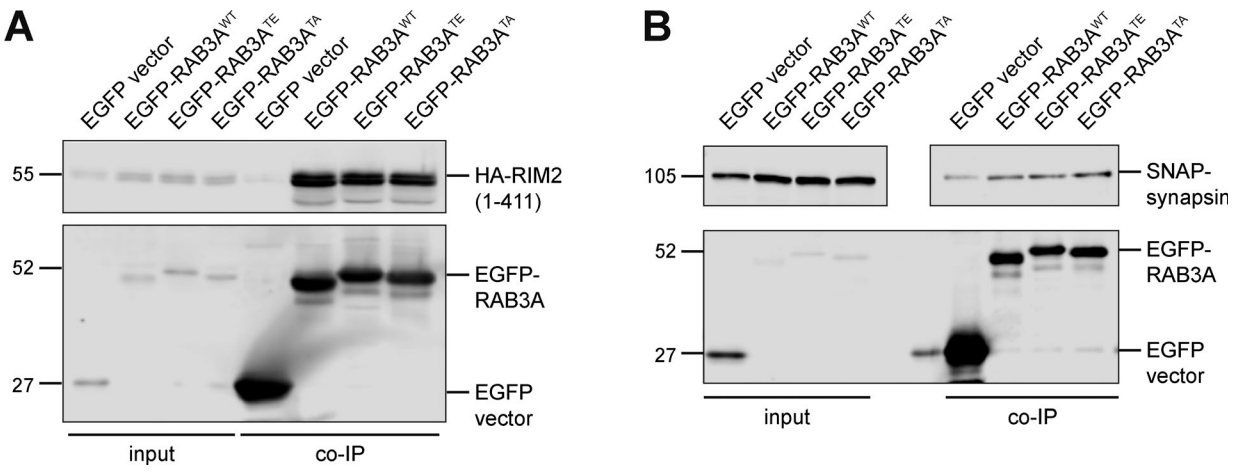

Figure S4. **Related to** Fig. 5**. (A)** Example immunoblot of RIM2 (first 411 residues) coimmunoprecipitation by RAB3A^{WT}, RAB3A^{TE}, or RAB3A^{TA}, coexpressed in HEK293T cells. **(B)** Example immunoblot of synapsin coimmunoprecipitation by RAB3A^{WT}, RAB3A^{TE}, or RAB3A^{TA}, coexpressed in HEK293T cells. Upper panel is separated for alignment purposes; no lanes that included sample were excluded. For all co-IP experiments shown, samples were processed and immunoblotted in parallel. Source data are available for this figure: SourceData FS4.

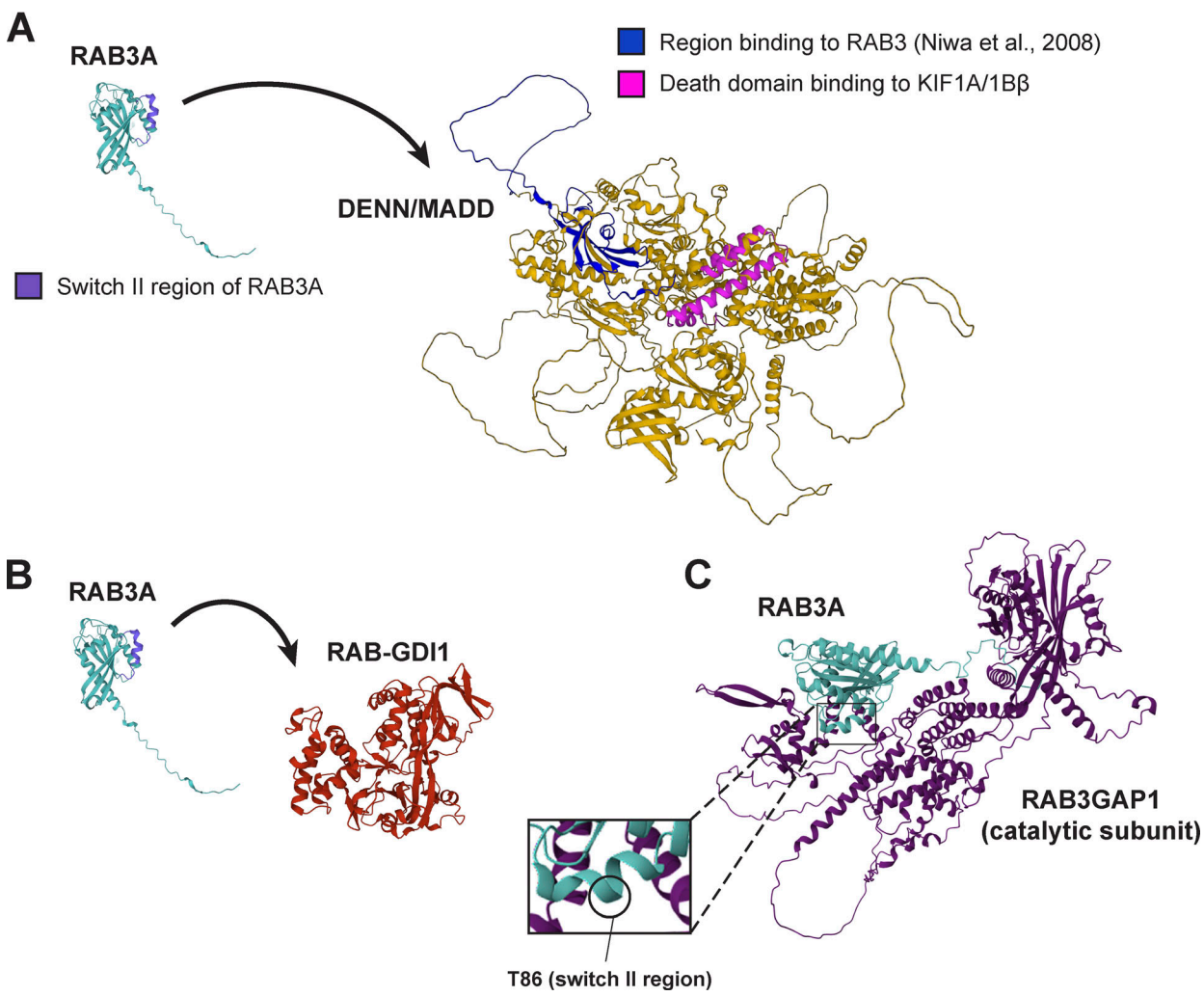

Figure S5. **Related to** Figs. 4 and 5**. (A)** AlphaFold predictions (Jumper et al., 2021; Varadi et al., 2022) of RAB3A and MADD. Left, annotated in purple: Putative switch II region of RAB3A (Singh et al., 2023). Right, annotated in blue: The N-terminal 161 residues that were previously shown (Niwa et al., 2008) to be necessary and sufficient for binding to RAB3. Right, annotated in magenta: The death domain toward the C-terminus of MADD that has been shown to be the motor-binding region (Niwa et al., 2008; Hummel and Hoogenraad, 2021). **(B)** AlphaFold predictions (Jumper et al., 2021; Varadi et al., 2022) of RAB3A and RAB-GDI1. **(C)** AlphaFold-Multimer (Jumper et al., 2021; Varadi et al., 2022; Evans et al., 2022, *Preprint*; Cianfrocco et al., 2017a, 2017b) prediction of complex formed by RAB3A and RAB3GAP1, the catalytic subunit of RAB3GAP. ipTM + pTM score for this prediction: 0.79404.